Caveolin-1 protects endothelial cells from extensive expansion of transcellular tunnel by stiffening the plasma membrane

Camille Morel, Eline Lemerle, Feng-Ching Tsai, Thomas Obadia, Nishit Srivastava, Maud Marechal, Audrey Salles, Marvin Albert, Caroline Stefani, Yvonne Benito, et al.

To cite this version:

Camille Morel, Eline Lemerle, Feng-Ching Tsai, Thomas Obadia, Nishit Srivastava, et al.. Caveolin-1 protects endothelial cells from extensive expansion of transcellular tunnel by stiffening the plasma membrane. 2023. pasteur-04364908v1

HAL Id: pasteur-04364908
https://hal.science/pasteur-04364908v1

Preprint submitted on 29 Oct 2023 (v1), last revised 4 Jan 2024 (v2)

HAL is a multi-disciplinary open access archive for the deposit and dissemination of scientific research documents, whether they are published or not. The documents may come from teaching and research institutions in France or abroad, or from public or private research centers.

L'archive ouverte pluridisciplinaire **HAL**, est destinée au dépôt et à la diffusion de documents scientifiques de niveau recherche, publiés ou non, émanant des établissements d'enseignement et de recherche français ou étrangers, des laboratoires publics ou privés.

Copyright

bioRxiv preprint doi: https://doi.org/10.1101/2022.09.27.509635; this version posted September 1, 2023. The copyright holder for this preprint (which was not certified by peer review) is the author/funder. All rights reserved. No reuse allowed without permission.

Caveolin-1 protects endothelial cells from extensive expansion of transcellular tunnel by stiffening the plasma membrane

Authors

Camille Morel[1], Eline Lemerle[2], Feng-Ching Tsai[3], Thomas Obadia[4,5], Nishit Srivastava[6], Maud Marechal[1], Audrey Salles[7], Marvin Albert[8], Caroline Stefani[9], Yvonne Benito[10], François Vandenesch[11], Christophe Lamaze[12], Stéphane Vassilopoulos[2], Matthieu Piel[6], Patricia Bassereau[3], David Gonzalez-Rodriguez[13], Cécile Leduc[14*], Emmanuel Lemichez[1*]

Affiliations

[1] Institut Pasteur, Université Paris Cité, CNRS UMR6047, INSERM U1306, Unité des Toxines Bactériennes, Département de Microbiologie, F-75015 Paris, France.

[2] Sorbonne Université, INSERM UMR U974, Institut de Myologie, Centre de Recherche en Myologie, F-75013 Paris, France.

[3] Institut Curie, PSL Research University, CNRS UMR168, Laboratoire Physico-Chimie Curie, F-75005 Paris, France.

[4] Institut Pasteur, Université Paris Cité, Bioinformatics and Biostatistics Hub, F-75015 Paris, France.

[5] Institut Pasteur, Université Paris Cité, G5 Infectious Diseases Epidemiology and Analytics, F-75015, Paris, France.

[6] Institut Curie and Institut Pierre Gilles de Gennes, PSL Research University, Sorbonne University, CNRS UMR144, F-75005 Paris, France.

[7] Institut Pasteur, Université de Paris Cité, Unit of Technology and Service Photonic BioImaging (UTechS PBI), C2RT, F-75015 Paris, France.

[8] Institut Pasteur, Université Paris Cité, Image Analysis Hub, F-75015 Paris, France.

[9] Benaroya Research Institute at Virginia Mason, Department of Immunology, Seattle, USA.

[10] Centre National de Référence des Staphylocoques, Hospices Civils de Lyon, Lyon, France

bioRxiv preprint doi: https://doi.org/10.1101/2022.09.27.509635; this version posted September 1, 2023. The copyright holder for this preprint (which was not certified by peer review) is the author/funder. All rights reserved. No reuse allowed without permission.

[11] CIRI, Centre International de Recherche en Infectiologie, Université de Lyon, Inserm U1111, Université Claude Bernard Lyon 1, CNRS UMR5308, ENS de Lyon, Lyon, France

[12] Institut Curie, PSL Research University, INSERM U1143, CNRS UMR3666, Membrane Mechanics and Dynamics of Intracellular Signaling Laboratory, F-75005 Paris, France.

[13] Université de Lorraine, LCP-A2MC, F-57000 Metz, France.

[14] Université Paris Cité, Institut Jacques Monod, CNRS UMR7592, F-75013 Paris, France.

*: corresponding authors: emmanuel.lemichez@pasteur.fr and cecile.leduc@ijm.fr

bioRxiv preprint doi: https://doi.org/10.1101/2022.09.27.509635; this version posted September 1, 2023. The copyright holder for this preprint (which was not certified by peer review) is the author/funder. All rights reserved. No reuse allowed without permission.

Abstract

Large transcellular pores elicited by bacterial mono-ADP-ribosyltransferase (mART) exotoxins inhibiting the small RhoA GTPase compromise the endothelial barrier. Recent advances in biophysical modeling point towards membrane tension and bending rigidity as the minimal set of mechanical parameters determining the nucleation and maximal size of transendothelial cell macroaperture (TEM) tunnels induced by bacterial RhoA-targeting mART exotoxins. We report that cellular depletion of caveolin-1, the membrane-embedded building block of caveolae, and depletion of cavin-1, the master regulator of caveolae invaginations, increase the number of TEM per cell. The enhanced nucleation of TEM correlates with a reduction of cell height, due to the increase of cell spreading and decrease of cell volume, which, together with the disruption of RhoA-driven F-actin meshwork, favor membrane apposition for TEM nucleation. Strikingly, caveolin-1 specifically controls the opening speed of TEMs leading to their dramatic 5.4-fold larger widening. Consistent with the increase of TEM density and width in siCAV1 cells, we record a higher lethality in caveolin-1-deficient mice subjected to a catalytically active mART exotoxin targeting RhoA during staphylococcal bloodstream infection. Combined theoretical modeling with independent biophysical measurements of plasma membrane bending rigidity point toward a specific contribution of caveolin-1 to membrane stiffening in addition to the role of cavin-1/caveolin-1-dependent caveolae in the control of membrane tension homeostasis.

bioRxiv preprint doi: https://doi.org/10.1101/2022.09.27.509635; this version posted September 1, 2023. The copyright holder for this preprint (which was not certified by peer review) is the author/funder. All rights reserved. No reuse allowed without permission.

Introduction

The endothelial cell monolayer lining the inner surface of the vascular tree forms an active semipermeable barrier that actively responds to hemodynamic forces to control blood pressure (1,2). Regulation of the endothelial barrier involves a bidirectional interplay between actomyosin cytoskeleton and plasma membrane mechanics, which together control paracellular exchanges at cell–cell junctions (3), as well as transcellular exchanges through less-characterized transcellular openings (1,2,4). Defining how membrane mechanical parameters affect the dynamics of opening and widening of transendothelial pores will help to better define the role of these openings both physiological and pathophysiological processes.

Large transcellular pores in the endothelium can contribute to aqueous humor outflow in the eyes, can form during the diapedesis of leukocytes, or appear when endothelial cells are intoxicated by several bacterial toxins known to breach the endothelial barrier (5–7). Bacterial mono-ADP-ribosyltransferases (mART) exotoxins, which catalyze the post-translational modification of the small GTPase RhoA for inhibition, induce the spontaneous formation of TEM tunnels up to 10 to 20 µm in diameter (8–10). This group of mART includes the exotoxin C3 (ExoC3) from *Clostridium botulinum*, and the Epidermal Differentiation Inhibitors (EDIN) A, B, and C close homologues from *Staphylococcus aureus* (11–13). The intravenous injection of EDIN or ExoC3 triggers vascular leakage (8,14). Cumulative evidence also indicates that EDIN favors the translocation of *S. aureus* through vascular tissues for dissemination (15,16). Although TEM tunnels have not yet been visualized *in vivo*, they form *ex vivo* in the endothelium lining the inner surface of rat aortas either infected with *S. aureus*-producing the RhoA-targeting EDIN mART or treated with EDIN (8). Mechanistically, the inhibition of RhoA signaling by bacterial mART exotoxins disrupts contractile actomyosin stress fibers, which otherwise stiffen in response to shear forces exerted by the blood flow that tends to compress cells (8–12). In line with this, compressive mechanical forces applied to the apical region of endothelial cells bring into close contact the apical and basal plasma membranes to nucleate transcellular pores (17). Although force-induced nucleation of TEMs can be triggered in the absence of inhibition of RhoA, the magnitude of the force required to mechanically open TEMs dramatically decreases when RhoA is inhibited (17). This led to postulate that TEMs form because of a disruption of actomyosin stress fibers under the control of RhoA, which concur to reduce the height of cells as they spread out (8,18). The physical mechanisms that set both the nucleation of TEMs and their maximal width remain to be ascertained experimentally.

bioRxiv preprint doi: https://doi.org/10.1101/2022.09.27.509635; this version posted September 1, 2023. The copyright holder for this preprint (which was not certified by peer review) is the author/funder. All rights reserved. No reuse allowed without permission.

TEMs represent a remarkable model system to identify the molecular machinery that controls cell mechanics (9). Our current view of the mechanical forces at play in the opening of TEMs largely arises from the phenomenological analogy drawn between TEM tunnel opening and the formation of dry patches in viscous liquid forced to spread on a solid surface, a physical phenomenon referred to as liquid dewetting (19). Notably, the analogy drawn between liquid and cellular dewetting suggests that the increase of membrane tension in response to cell spreading is the driving force of TEM nucleation also contributing to define the initial speed of opening, i.e. before that membrane tension relaxation around TEM edges and build-up of an actomyosin bundle encircling TEMs counteract the opening (10,19,20). Of note, the high curvature of the plasma membrane at the edge of TEMs also points toward a contribution of membrane bending rigidity in their dynamics. Experimental evidence is still required to ascertain roles of membrane tension and bending rigidity in the dynamics of TEM tunnel nucleation and enlargement.

Caveolae are mechano-regulators of the plasma membrane that spontaneously flatten to accommodate acute mechanical loads and thereby prevent membrane rupturing (21,22). Caveolin oligomers are essential components of caveolae pits (23,24). Caveolin-1 homo-oligomers form flat discoid complexes embedded into the inner leaflet of the membrane (24). The process of invagination of caveolar pits of 50-100 nm diameter involves the association of caveolin-1 with cavin-1 cytosolic structural protein (also referred to as PTRF) (25–29). Caveolae pits are further stabilized at their neck by the assembly of a ring of dynamin-like EHD2 oligomers (30–32). In endothelial cells, the crosstalk between caveolin-1 and RhoA during actomyosin contractility leads to critical mechano-sensing and adaptation to hemodynamic forces (33,34). For example, caveolin-1-deficient mice undergo an increase in the endothelial nitric oxide (eNOS) signaling that is critical to activate RhoA signaling via nitration-mediated inhibition of the GTPase activating protein (GAP) activity of p190RhoGAP-A (35–37). Cell biology and epidemiological studies have started to establish the importance of caveolin-1 in host–pathogen interactions (38–40). Considering the protective function of caveolae membrane invaginations in ensuring membrane tension homeostasis in response to acute mechanical loads (21,41), caveolin-1 and cavin-1 represent potential mechano-regulators of transcellular pore dynamics.

bioRxiv preprint doi: https://doi.org/10.1101/2022.09.27.509635; this version posted September 1, 2023. The copyright holder for this preprint (which was not certified by peer review) is the author/funder. All rights reserved. No reuse allowed without permission.

Using cutting edge microscopy technics, we establish that endothelial cells treated with RhoA-targeting mART display caveolae pits at the ventral part of the plasma membrane and a loose F-actin meshwork that frame large cytosolic zones devoid of F-actin. We report that the disruption of caveolae and depletion of caveolin-1, using siRNA-targeting cavin-1 or caveolin-1, respectively increases the number of TEM per cell. We establish that the increase of TEM opening correlates with a decrease in cell volume concomitant with cell spreading, which concur to a decrease in cell height. Strikingly, we establish that caveolin-1, contrary to cavin-1, controls the widening of TEMs which rule out a role of caveolae membrane-invaginations. This increase in both the number and width of TEMs correlates with a higher susceptibility of caveolin-1-deficient mice to the lethal effect of EDIN-B mART activity during *S. aureus* septicemia. Finally, using an independent biophysical technique and theoretical modeling, we provide compelling evidence that caveolin-1 contributes, independently of cavin-1, to increasing plasma membrane bending rigidity. These data point for a role of cavin-1/caveolin-1 components of caveolae in the regulation of TEM nucleation through the modulation of membrane tension. Hence, we ascribe to caveolin-1 a function in stiffening the plasma membrane that is independent from cavin-1-dependent caveolae, which eventually modulates TEMs opening speed and width.

bioRxiv preprint doi: https://doi.org/10.1101/2022.09.27.509635; this version posted September 1, 2023. The copyright holder for this preprint (which was not certified by peer review) is the author/funder. All rights reserved. No reuse allowed without permission.

Results

Caveolae control the density of TEM tunnels.

Formation of large transendothelial cell macroaperture (TEM) tunnels is observed in endothelial cells intoxicated with EDIN-like factors from *S. aureus*, as well as with the prototypic exoenzyme C3 (ExoC3) from *C. botulinum.* Considering that RhoA inhibition increases endothelial cell spreading, we investigated the impact of ExoC3 treatment on the distribution and density of caveolae in the inner leaflet of the plasma membrane in human umbilical vein endothelial cells (HUVECs) (Fig. 1A-C). We used a cell unroofing approach that allows direct visualization of membrane invaginations on a platinum replica via transmission electron microscopy (42). In both naïve and ExoC3-treated cells, we observed membrane-associated cytoskeleton filaments, the honeycomb structure of clathrin lattices, clathrin-coated pits, and rough aspects of pit-like caveolar invaginations (Fig. 1A). We verified that the treatment of cells with ExoC3 had no impact on caveolin-1 and cavin-1 expression (Fig. S1A). Of note, the density of the cytoskeletal filaments was less pronounced in the ExoC3-treated cells (Fig. 1D, arrowhead). Cells were transfected with a plasmid encoding GFP-caveolin-1 to confirm by immunogold labelling the presence of caveolin-1-positive caveolae invaginations at the ventral side of the plasma membrane (Fig. 1B). We quantified the density of caveolae in ExoC3-treated and control cells. In total, we analyzed an area $A_{\text{area}} > 175\ \mu m^2$ under each condition ($n \geq 16$ membrane areas of independent cells per condition). We recorded a 1.6-fold decrease in the mean density of caveolae in the ExoC3-treated cells, which exhibited 3.4 ± 2.1 caveolae/μm^2 of membrane, as compared to 5.4 ± 3.1 caveolae/μm^2 of membrane in untreated cells (Fig. 1C). The pool of plasma membrane-located caveolae remaining in ExoC3-treated cells are evenly distributed with no detectable accumulation around TEM tunnels (Fig. 1B). ExoC3 treatment reduces the density of invaginated caveolae at the plasma membrane, pointing for the interest of studying the impact of caveolae depletion in TEM formation.

Before functional analysis of the impact of caveolae components on TEM tunnel nucleation and growth, we analyzed the previously established stoichiometry of caveolin-1 and cavin-1 in response to siRNA treatments (43). We observed that small interfering RNA (siRNA)-mediated depletion of caveolin-1 (siCAV1) strongly reduces both caveolin-1 and the cellular pool of cavin-1/PTRF by approximately 80% (Fig. S1B). In contrast, about one half of the pool of caveolin-1 remained unaffected by the siRNA-targeted depletion of cavin-1/PTRF (siPRTF)

bioRxiv preprint doi: https://doi.org/10.1101/2022.09.27.509635; this version posted September 1, 2023. The copyright holder for this preprint (which was not certified by peer review) is the author/funder. All rights reserved. No reuse allowed without permission.

(Fig. S1B). We concluded that siPTRF leaves a cellular pool of caveolin-1 unaffected, contrary to siCAV1. Both siRNA treatments had no effect on the extent of mono-ADPribosylation of RhoA (Fig. S1C). We next quantified the efficiency of TEM tunnel formation in different conditions of siRNA treatment. HUVECs were treated with siCTRL, siCAV1 or siPTRF prior to ExoC3 treatment. Examples of cells treated in these conditions are shown in Figure 1D and in supplementary videos 1, 2 and 3. Quantitative measurements showed a higher percentage of cells displaying at least one TEM in the population of caveolin-1 or cavin-1-deficient cells (37.6 ± 1.3% siCAV1 and 36.4 ± 1.3% siPTRF versus 28.8 ± 1.2% siCTRL) (Fig. 1E). Moreover, we observed a significant increase in the density of TEM per cell in siCAV1 ($N_{\mathrm{TEM\_siCAV1}} = 1.96$) and siPTRF ($N_{\mathrm{TEM\_siPTRF}} = 1.36$) conditions, as compared to siCTRL ($N_{\mathrm{siCTRL}} = 0.91$) (Fig. S2A). We verified that such an increase of TEM density per cell and within the cell population was also induced by the ExoC3-like RhoA-targeting mART EDIN from *S. aureus* (Fig. S2B-C) or by siRNA-targeting EHD2 caveolae-stabilizing protein, a treatment that leaves caveolin-1 and cavin-1 unaffected (Fig. S3). Together, these data show that the efficiency of formation of TEMs is inversely correlated to the density and stability of caveolae at the plasma membrane.

Caveolae buffer the decrease of cell height triggered by RhoA inhibition-driven spreading.

Formation of TEMs due to the disruption of RhoA-driven F-actin polymerization and actomyosin contraction is facilitated by a reduction in cell height that promotes contact between the apical and basal membranes (17,18,29). We first quantified the mesh size of F-actin network using 2D stochastic optical reconstruction microscopy (STORM) that integrates F-actin signals with a ~30-nm resolution over the whole cell thickness which can be as thin as 50 nm at the cell periphery (10). The siCTRL, siCAV1 and siPTRF-transfected HUVECs displayed a classical organization of actin cytoskeleton with actin stress fibers intertwined with a high-density meshwork of F-actin (Fig. 2A, control). When siRNA-treated cells were next intoxicated with ExoC3, we observed the disruption of actin stress fibers together with a reorganization of the actin cytoskeleton into a loosely intertwined and irregular F-actin meshwork defining large zones devoid of F-actin (Fig. 2A, ExoC3). In all conditions of siRNA treatment, we have measured that ExoC3 treatment induces a significant increase of actin-mesh size of about 0.2 μm^2, as compared to non-intoxicated cells (Fig. 2B). No significant difference of mesh size was recorded between siCTRL, siCAV1 or siPTRF conditions before and after treatment with ExoC3 (Fig. 2B). We concluded that in addition to the well-establish impact of

bioRxiv preprint doi: https://doi.org/10.1101/2022.09.27.509635; this version posted September 1, 2023. The copyright holder for this preprint (which was not certified by peer review) is the author/funder. All rights reserved. No reuse allowed without permission.

RhoA inhibition on actin stress fibers it generates a loose F-actin meshwork framing large cellular zones devoid of F-actin of same extent in all siRNA conditions.

We next investigated the role played by caveolin-1 and cavin-1 in the control of the cell height (*h*), an essential parameter in TEM nucleation. The mean value of this cell shape parameter is proportional to the ratio between the volume (*V*) and spreading area (*A*) of cells (Table 1). The spreading area was estimated from the measurement of cell contours (Fig. 3A). The volume of cells was quantified by fluorescent dye exclusion, as depicted in Fig. 3B, and as previously described (44). Upon intoxication of siCTRL-treated cells, we recorded a significant increase of 36% of the spreading area together with 17% increase of the cell volume (Fig. 3C-3D and Table 1). The dominant impact of cell area changes over the volume parameter accounts for the calculated decrease of cell height of 15% (Table 1). Hence, when siCAV1- and siPTRF-transfected cells were treated with ExoC3, we recorded a reduction of cell volume concomitant to the increase in their spreading area (Fig. 3C-3D and Table 1). The reinforced reduction in cell height recorded in siCAV1 or siPTRF-treated cells is in good agreement with our findings showing that these treatments increase the density of TEMs. Note that in the absence of ExoC3, we recorded that the effects of siPTRF on cell shape parameters were slightly stronger than those of siCAV1, thereby highlighting the key involvement of caveolae in the control of cell height (Fig. 3C-3D). The depletion of caveolae and the inhibition RhoA work together to reduce cell height that favors together with the loss of F-actin the nucleation of TEMs.

Caveolin-1 and cavin-1 have a different impact on TEM expansion dynamics.

Since the TEM opening is transient, we next characterized the impact of caveolin-1 and cavin-1 in TEM dynamics that allow to define TEM maximal width. We implemented a pipeline of live-cell imaging and semi-automatic analysis that relies on the detection of Lifeact-GFP signal around TEMs to segment the opening area (18). Figure 4A shows the projections of the first image recorded for each TEM that formed over 1-hour recording (Fig. 4A). We see that TEM tunnels preferentially open at the cell periphery where the cell height is minimal (Fig. 4A). We then measured the maximal values of each TEM areas over 1 hour of video recording (Fig 4B), as well as the speeds of opening and closure (Fig 4C). Interestingly, we recorded 5.4-fold wider TEMs in siCAV1-treated cells, as compared to siPTRF- and siCTRL-treatments (Fig. 4A and 4B). Interestingly, the time for TEMs to reach their maximal diameter (t_{max}) and the overall TEM cycles (t_c) remain identical in all conditions (Fig. 4C). Thus, TEMs became wider in siCAV1 condition in absence of change in the time frame of opening, suggesting that caveolin-1 controls the speed of opening. To capture initial values of TEM opening speed (S_o) we used

bioRxiv preprint doi: https://doi.org/10.1101/2022.09.27.509635; this version posted September 1, 2023. The copyright holder for this preprint (which was not certified by peer review) is the author/funder. All rights reserved. No reuse allowed without permission.

a 15-fold higher temporal resolution, i.e. using a video recording of 1 image per second. Strikingly, we recorded a 2-fold higher opening speed in caveolin-1-depleted cells: S_{o_siCAV1}=2.4 µm^2/s versus S_{o_siCTRL}=1.1 µm^2/s in control cells, which contrasts with the lack of impact of siPTRF (Fig. 4D). In conclusion, we have identified a specific function of caveolin- 1 in the regulation of the opening speed of TEMs that has a critical impact on TEM maximal width.

Loss of caveolin-1 sensitizes mice to EDIN-B lethal effects during *S. aureus* sepsis.

We reasoned that the increased density and width of TEMs triggered by the cellular depletion of caveolin-1 should result in higher susceptibility of caveolin-1 (Cav1)-deficient (CAV1$^{-/-}$) mice to the inhibition of RhoA by EDIN-like mART exotoxins during bloodstream infection by *S. aureus*. This would establish caveolin-1 as a resistance factor in the pathogenicity triggered by EDIN-like factors from *Staphylococcus aureus*. To address this question, we first established the susceptibility of CAV1$^{-/-}$ mice and wildtype littermates (CAV1$^{+/+}$) to *S. aureus* strain LUG1799 (WT *edinB*) in a model of septicemia (Fig. 5A). LUG1799 belongs to the European lineage ST80 derived from community-acquired methicillin-resistant *S. aureus*, which expresses EDIN-B mART exotoxin (EDIN-B) (16). We first monitored over a period of 7 days the survival of CAV1$^{-/-}$ and CAV1$^{+/+}$ mice challenged with three increasing *inocula* of WT *edinB*. All the mice, except one CAV1$^{-/-}$ mouse, recovered from infection triggered with 5 $\times 10^6$ CFU of bacteria/mouse (CFU/m), while all mice died 24 hours after intravenous injection of 5×10^8 CFU/m. In contrast, when mice were challenged with an intermediate dose of WT *edinB* of 5×10^7 CFU/m, we recorded a higher lethality of CAV1$^{-/-}$ as compared to CAV1$^{+/+}$ mice ($P < 0.001$, Mantel–Cox test). All the CAV1$^{-/-}$ mice died on day 1 post-challenge, whereas the death of CAV1$^{+/+}$ occurred with a delay of 1 to 2 days, with one CAV1$^{+/+}$ mouse surviving (Fig 5A, 5×10^7 CFU/m). The loss of caveolin-1 expression thus sensitizes mice to bloodstream infection triggered by *S. aureus*-produced EDIN-B. We then explored the pathogenic effect of EDIN-B mART activity of RhoA. In control experiments with CAV1$^{+/+}$ mice infected with either WT *edinB* or Δ*edinB* strains, we saw no difference of susceptibility between the strains and despite a broad range of 4 different *inocula* tested (Fig. S4). In this set experiments, we identify the lethal dose 50 (LD_{50}) at 2.5×10^7 CFU/m with both strains of *S. aureus*. When we challenged CAV1$^{-/-}$ mice with this LD_{50} of *S. aureus* (2.5×10^7 CFU/m) we saw a lower survival with *S. aureus* WT *edinB* (*n*=11 death /18 mice), as compared to Δ*edinB* (*n*=4 death /17 mice) ($P = 0.0123$, Mantel–Cox test) (Fig. 5C). To provide a causal link between the pathogenicity of EDIN-B recorded in CAV1$^{-/-}$ mice and the inhibition of RhoA catalyzed by EDIN-B, we

bioRxiv preprint doi: https://doi.org/10.1101/2022.09.27.509635; this version posted September 1, 2023. The copyright holder for this preprint (which was not certified by peer review) is the author/funder. All rights reserved. No reuse allowed without permission.

performed a similar experiment with *S. aureus* Δ*edinB* complemented with a plasmid expressing either WT EDIN-B (Δ*edinB* pEDIN-B) or the catalytically inactive mutant EDIN-B-RE (Δ*edinB* pEDIN-B-RE). We saw a significant decrease of survival in caveolin-1-deficient mice infected with Δ*edinB* pEDIN-B, as compared to mice infected with Δ*edinB* pEDIN-B-RE. We concluded that in the context of bloodstream infection by *S. aureus*, caveolin-1 expression confers a resistance to the pathogenicity triggered by EDIN-B mART activity on RhoA.

Differential impacts of caveolin-1 and cavin-1 on membrane rigidity

Since we expect that S_o depends on membrane mechanical parameters (see the physical model description in the Materials and Methods), this suggests that caveolin-1, but not cavin-1 modulates TEM opening speed by affecting membrane mechanics. We then inferred changes in membrane mechanical properties upon depletion of caveolin-1 or cavin-1, using a refined theoretical model of cellular dewetting. This model accounts for the presence of several TEMs opening simultaneously (see the physical model description in the Materials and Methods). Importantly, the model is based on the hypothesis that plasma membrane deformation, enabling TEM nucleation and tunnel growth, is a function of membrane tension and bending rigidity, assuming a limited contribution of membrane adhesion to cortical cytoskeleton (45). Indeed, consistent with this hypothesis of a minimal impact of cortical cytoskeleton elements on membrane mechanics, the 2D STORM images (Fig. 2A) established a massive disruption of the dense F-actin meshwork in ExoC3-treated cells, leaving large cellular zones devoid of F-actin. As explained in the Materials and Methods section in detail, the model predicts that the initial opening speed S_o is proportional to the membrane tension, consistent with a critical role of membrane tension in TEM growth (9). From our measurements, we deduce that cells treated with siCAV1 have a significant 2-fold higher membrane tension than the controls, and no effect in siPTRF-treated cells (see Methods). Moreover, according to the model, the maximum TEM size R_{max} depends strongly on membrane bending rigidity but weakly on the initial membrane tension. Thus, from our R_{max} measurements, the model allows the estimation of the bending rigidities κ in the different conditions. Using the following values for the siCTRL-treated cells - an initial membrane tension σ_0=2.5 10^{-5} N/m (46) and a bending rigidity κ_{siCTRL}=23.4 k_BT (direct measurement, see below) – the model predicts a 55% reduction of membrane rigidity from a loss of expression of caveolin-1 and a lower reduction of 15% upon a loss of cavin-1 expression as compared to caveolin-1.

bioRxiv preprint doi: https://doi.org/10.1101/2022.09.27.509635; this version posted September 1, 2023. The copyright holder for this preprint (which was not certified by peer review) is the author/funder. All rights reserved. No reuse allowed without permission.

To test these predictions, we used an independent approach to measure the membrane bending rigidity in different conditions of cell treatment. This quantitative method is based on pulling membrane tethers from cell-derived plasma membrane spheres (PMSs) that are devoid of F-actin cortex and preserve the lipid membrane (Fig. 6A) (21,47,48). PMSs prepared from untreated siCTRL-, siCAV1- and siPTRF-treated HUVECs were aspirated into a micropipette, allowing to control membrane tension. Membrane tethers were pulled from PMSs using optical tweezers (47). The force, f, exerted on the membrane tether can be measured as function of membrane tension (σ); it also depends on the bending rigidity (κ) following $f = 2\pi\sqrt{2\kappa\sigma}$ (Fig. 6B-C) (49). Thus, the analysis of the slope of f^2 versus σ provides a measurement of the membrane bending rigidity of a PMS (Fig. 6D). We measured a significant decrease of 30% of the bending rigidity from κ_{siCTRL}=23.4 ± 0.9k_BT to κ_{siCAV1}=17.0 ± 0.9 k_BT. Moreover, we observed no significant difference in siPTRF conditions, as compared to siCTRL, with a κ_{siPTRF}=23.4 ± 1.3 k_BT (Fig. 6D). In good agreement with the theoretical predictions, these measurements establish that the expression of caveolin-1, but not of cavin-1, significantly stiffens the plasma membrane.

bioRxiv preprint doi: https://doi.org/10.1101/2022.09.27.509635; this version posted September 1, 2023. The copyright holder for this preprint (which was not certified by peer review) is the author/funder. All rights reserved. No reuse allowed without permission.

Discussion

We report that siRNA-mediated knockdown of key structural and regulatory components of caveolae sensitizes endothelial cells to the formation of TEM tunnels triggered by the inhibition of RhoA-driven actomyosin contractility. Hence, inhibition of RhoA reduces by 2-fold the pool of caveolae invaginations at the plasma membrane. Mechanistically, we report that targeted depletion of caveolin-1 and cavin-1 caveolae decreases cell volume and increases cell spreading, which concur to decrease the height of cells favoring membrane apposition for TEM nucleation. Strikingly, we establish a specific role for caveolin-1 in controlling the opening speed of TEMs that has a dramatic impact on TEM size. In good agreement with the recorded increase of TEM formation and width following caveolin-1 knockdown, we establish a higher susceptibility of Cav1-deficient mice to lethal effects triggered by EDIN-B mART during staphylococcal bloodstream infection. Finally, we provide theoretical and experimental evidence that in addition to the well-established role of caveolae in membrane tension homeostasis, caveolin-1 rigidifies plasma membrane.

Our biophysical measurements unravel that caveolin-1 depletion decreases membrane bending rigidity by 30%, while depletion of cavin-1 has no impact. This experimental value is of the same order of magnitude as the 55% decrease in bending rigidity inferred from the cell dewetting model. The difference recorded between these approaches can be attributed to several approximations in the theoretical model, notably the simplified treatment of the physical membrane tension variation, of the cytoskeletal contributions, and of the interactions between neighboring TEM tunnels. Note that the formation of the actin cables around the TEM before it reaches full size saturation may also limit the correct estimation of the bending rigidity (20). The mechanical role of caveolin-1 reported here is highly significant considering that previous studies showed that inclusion of integral proteins in membranes had no impact on bending rigidity, as shown in the bacteriorhodopsin experiments (50), or even decreased membrane rigidity as reported for the Ca^{2+}-ATPase SERCA (51). Previous simulations have also confirmed the softening effect of protein inclusions (52). Nevertheless, our observations can be explained by a high density of stiff inclusions in the plasma membrane (>>10%), which was generally not achievable with the reconstituted membranes described in the above-mentioned references. Caveolin-1 expression may also contribute to plasma membrane stiffening by interacting with membrane-associated components of the cortical cytoskeletal or by structuring ordered lipid domains. Nevertheless, it has been reported that the Young’s modulus of the cell

bioRxiv preprint doi: https://doi.org/10.1101/2022.09.27.509635; this version posted September 1, 2023. The copyright holder for this preprint (which was not certified by peer review) is the author/funder. All rights reserved. No reuse allowed without permission.

cortex dramatically decreases in ExoC3-treated cells (17) suggesting a small additional contribution of caveolin-1 depletion to membrane softening. This is supported by 2D STORM data showing a dramatic reorganization of actin cytoskeleton in ExoC3-treated cells into a loose F-actin meshwork that is not significantly exacerbated by caveolin-1 depletion. Regarding the link between caveolin-1 and lipids it is well established that caveolae are enriched with cholesterol, sphingomyelin, and glycosphingolipids, including gangliosides (53,54), which are known to rigidify membranes (55). Thus, caveolin-1 might contribute to the enrichment of the plasma membrane with these lipid species. We did not establish experimental conditions allowing us to deplete cholesterol without compromising the shape of HUVECs, which prevented a proper analysis of TEM dynamics. Moreover, a previous attempt to increase TEMs width by softening the membrane through the incorporation of poly-unsaturated acyl chains into phospholipids failed, likely due to homeostatic adaptation of the membrane’s mechanical properties (18). Further studies are required to establish whether and how caveolin-1 oligomers control membrane mechanical parameters through modulation of lipids organization or content.

Our data establish a function to cavin-1-dependent caveolae in the regulation cell height. Indeed, we measured an increase in cell spreading and a decrease in cell volume upon depletion of caveolin-1 or cavin-1, which are essential components of caveolae. This is consistent with findings showing that cell homeostasis during spreading is achieved by decreasing cell volume. Such a coupling between variations in cell spreading area and cell volume is breached by disrupting cortical contractility, resulting in cell swelling (56). Consistently, we show that the ExoC3-triggered increase in endothelial cell spreading occurs concomitantly with a decrease in cell volume. This might be a consequence of the inhibition of RhoA signaling, which is permissive for the activity of volume-regulated anion channels (VRACs) (57). Here, we show that the decrease in cell volume upon depletion of cavin-1, and to a lesser extent after depletion of caveolin-1, occurs independently of RhoA signaling, i.e. in ExoC3-treated cells. Thus, how caveolae control the cellular volume once RhoA signaling is inhibited awaits determination. Our findings also suggest that depletion of caveolae and RhoA inactivation, may release membrane-folding driven mechanical constraints that would limit cell spreading. Another hypothesis is that caveolae control indirectly the cellular geometry via a documented function of cavin-1 on cell signaling (58–61).

The molecular basis of interindividual variability in *S. aureus* infections is unclear, although the expression of caveolin-1 has recently been suggested (39). Indeed, a human genetics study pinpointed the impact of haploinsufficiency of the OTULIN deubiquitinase in

bioRxiv preprint doi: https://doi.org/10.1101/2022.09.27.509635; this version posted September 1, 2023. The copyright holder for this preprint (which was not certified by peer review) is the author/funder. All rights reserved. No reuse allowed without permission.

sensitizing host cells to lysis triggered by the highly prevalent α-haemolysin pore-forming toxin of *S. aureus*, a major determinant in staphylococcal pneumonia (39). The defect in OTULIN activity led to an increase in caveolin-1 cellular protein levels in dermal cells, which in turn upregulates the expression of the ADAM10 receptor of alpha-haemolysin pore-forming toxin. Here, we report that caveolin-1 expression is not regulated by RhoA signaling. Furthermore, we establish that the loss of caveolin-1 expression sensitizes mice to the lethal effects triggered by EDIN-B mART activity on RhoA during *S. aureus* septicemia, thus ascribing a pathogenicity potential to this exotoxin that is counteracted by expression of caveolin-1. In line with this, a recent analysis of an observational cohort of patients with *S. aureus* community-acquired pneumonia indicated that EDIN-B, together with Panton–Valentin leukocidin, are positively associated with the etiology of hemoptysis, manifests by the presence of blood in sputum (62). Whether TEMs are involved in the etiology of hemoptysis remains to be investigated. Although we cannot argue that there is a causal link between the lethal effect of EDIN-B in caveolin-1-deficient animals and the protective function of caveolin-1 against TEM tunnel formation in endothelial cells, these findings represent a first step towards establishing that endothelial cells regulate TEM tunnel formation and width *in vivo*. Such a hypothesis is supported by previous findings showing that RhoA inhibition reduces paracellular permeability while dramatically increasing transcellular permeability, and that ADP-ribosyltransferases targeting RhoA increase vascular permeability to the point of animal death when TEM enlargement is no longer controlled (8,14). Collectively, these findings ascribe to variations in caveolin-1 expression a bidirectional impact on host susceptibility to *S. aureus* infection, pointing for a possible role of TEM tunnels.

bioRxiv preprint doi: https://doi.org/10.1101/2022.09.27.509635; this version posted September 1, 2023. The copyright holder for this preprint (which was not certified by peer review) is the author/funder. All rights reserved. No reuse allowed without permission.

Materials and Methods

Bacterial strains and culture conditions

S. aureus HT20020209-LUG1799, referred to as wild-type WT *edinB* in this study, is a minimally passaged ST80 *SCCmecIV* PVL+ MRSA strain isolated in France (deposited at http://www.ebi.ac.uk/ena) that is representative of ST80 CA-MRSA clones (63,64). *S. aureus* HT20020209-LUG1799 with the *edinB* gene deletion is referred to as Δ*edinB* in this study (16). The strain Δ*edinB* was complemented with a pMK4-pPROT plasmid expressing the wildtype form of EDIN-B to generate the strain Δ*edinB* pEDIN-B-WT or with pMK4-pPROT expressing the catalytically inactive mutant form of EDIN-B (EDIN-B-R185E) to generate the strain Δ*edinB* pEDIN-B-RE, as previously described (16). Both strains were grown in lysogeny broth (LB) with shaking at 200 rpm and 37 °C. Equal growth kinetics were verified (not shown).

Mouse infection model

Adult male and female B6.Cg-*Cav1*^{tm1Mls}/J mice (strain #: 007083, Jackson Laboratories) and C57BL/6J mice (Charles River) were housed under specific-pathogen-free conditions at the Institut Pasteur animal facilities licenced by the French Ministry of Agriculture (B75150102). Mice received food and water ad libitum, and their weight was recorded daily throughout the study. *S. aureus* strains were cultured in LB at 37 °C until reaching an $OD_{600} = 1$ after overnight culture. After washing twice in PBS, cell pellets were resuspended in sterile 0.9% NaCl. Infections were carried out by injecting 300 µL serial dilutions of inoculum intravenously into the tail vein of the mice. Animal survival was monitored daily.

Cell culture, transfection and toxicity

Primary human umbilical vein endothelial cells (HUVECs, PromoCell) were cultured in human endothelial serum-free medium (SFM, Gibco) containing 20% foetal bovine serum, 20 ng/ml FGF-2, 10 ng/ml EGF, and 1 µg/ml heparin and referred to as complete SFM (SFMc). Cells were cultured on gelatine-coated culture ware at 37 °C with 5% CO_2 for as many as six passages. For siRNA transfection, HUVECs were cultured at a density of 38,000 cells/cm^2. ON-TARGETplus smart pool siRNA (Dharmacon) targeting human caveolin-1 (L-003467-00-0005), EHD2 (L-016660-00-0005), cavin-1/PTRF (L-012807-02-0005) or control RNAi SR-CL000 (Eurogentec) was used at 100 nM via magnetofection technology (OZ Biosciences)

bioRxiv preprint doi: https://doi.org/10.1101/2022.09.27.509635; this version posted September 1, 2023. The copyright holder for this preprint (which was not certified by peer review) is the author/funder. All rights reserved. No reuse allowed without permission.

following the manufacturerʹs instructions in serum-free OptiMEM (Gibco). When necessary, cells were electroporated 24 h post-magnetofection and then used from 48 to 54 h post-magnetofection. HUVEC electroporation of plasmids encoding caveolin-1-GFP (21) or Lifeact-GFP (Ibidi, GmbH, Planegg/Martinsried, Germany) was performed as described in (65). Briefly, cells were trypsinized and resuspended in Ingenio Solution (Mirus) containing plasmid DNA (10 µg/10^6 cells) in a 4-mm cuvette (CellProjects). Cells were then electroporated at 300 V and 450 µF with one pulse of a GenePulser electroporator (Bio–Rad). Cells were incubated in SFMc, and the medium was replaced 3 h post-electroporation. Cells were treated 6 h post-electroporation. Recombinant ExoC3 and EDIN were produced in *E. coli* and purified as described in (8). Cells were treated with ExoC3 or EDIN exotoxins at a final concentration of 100 µM for 24 h.

Immunoblotting and Western blotting

Proteins were resolved on 12% SDS-polyacrylamide gels and transferred to nitrocellulose membranes (GE Healthcare). The primary antibodies used were mouse anti-EHD2 (L-05) (Santa Cruz sc-100724), rabbit anti-Cav1 (Cell Signaling Technology #3238), rabbit anti-PTRF (Proteintech, 18892-1-AP) and mouse anti-GAPDH (Santa Cruz sc-47724). The secondary antibodies used were HRP-conjugated anti-mouse or anti-rabbit (Dako). Signals were imaged using a Fujifilm LAS-3000 system and quantified with ImageJ software.

Immunofluorescence

HUVECs were seeded on a gelatine-coated µ-Dish 35 mm, high (Ibidi) and treated as indicated previously (20). Cells were fixed in ready-to-use paraformaldehyde, 4% in PBS (Bio–Rad). Immunostaining of fixed cells permeabilized in 0.5% Triton X-100 was performed. FITC-phalloidin or TRITC-phalloidin at 1 µg/ml (Sigma) were used to stain actin, and DAPI (Life Technologies) was used to label nuclei.

Video microscopy

HUVECs were electroporated with LifeAct-GFP-pCMV as described above and seeded on a gelatine-coated polymer coverslip dish (Ibidi). After treatment with ExoC3 (see above), the cells were supplemented with 25 mM HEPES (pH 7.4) and their proliferation was recorded at 37 °C with a Nikon T_i inverted microscope using an Ultraview spinning disk confocal system (Perkin Elmer). For determining TEM opening, images were taken every 10 to 25 seconds for

bioRxiv preprint doi: https://doi.org/10.1101/2022.09.27.509635; this version posted September 1, 2023. The copyright holder for this preprint (which was not certified by peer review) is the author/funder. All rights reserved. No reuse allowed without permission.

1 h. To determine the opening speed (S_o), images were taken every second for 30 min. Acquired videos were analysed via an ICY-based semiautomatic protocol.

Cell volume measurement

After siRNA treatment and other treatments, cells were seeded onto a PDMS chip (2.10^6 cells/mL) as described previously (44). Briefly, chambers were coated with 10 µg/ml fibronectin in PBS (Life Technologies) for 1 h at RT. Chambers were washed with medium before cell seeding. Cells were resuspended in medium supplemented with 0.5 mg/ml Alexa Fluor 488 dextran (MW 10 kD; Life Technologies) and then injected into the chamber. Finally, the chamber was immersed in medium to prevent evaporation. HUVECs were allowed to adhere for 4 to 6 h in SFMc at 37 °C with 5% CO_2 before acquisition.

Images were analysed with MATLAB (MathWorks). The intensity of the background was maximal in the absence of any object (I_{max}) and represented the fluorescence value for the maximal height of the chamber (h_{max}). In contrast, the pillar excludes fluorescence, which therefore reflects the minimal fluorescence intensity (I_{min}). At the cell level, the fluorescence was partially excluded at a given point for a cell at a given height ($h_{x,y}$). This strategy enables the measurement of the fluorescence intensity at this point ($I_{x,y}$). After calibrating the fluorescence intensity signal $\alpha = (I_{max} - I_{min})/h_{max}$, integration of the fluorescence intensity over the cell area provided the cell volume (V_{cell}):

$$V_{cell} = \iint_{x,y} \frac{\boldsymbol{Imax - Ix,y}}{\alpha}\, dxdy$$

Metal replicates and transmission electron microscopy

Metal replicates of the ventral plasma membranes of HUVECs cultured on glass coverslips were obtained by sonication according to a published protocol (42,66). Briefly, cells were rinsed three times with Ringer's buffer with Ca^{2+} and then briefly subjected to a concentration of 0.5 mg/mL poly-L-lysine diluted in Ca^{2+}-free Ringer's buffer (Sigma–Aldrich). Poly-L-lysine was removed by washing with Ca^{2+}-free Ringer's buffer. The coverslips were immersed in KHMgE buffer at 37 °C before sonication (Vibra-Cell VCX130 ultrasonic processor, Sonics) at a 20% amplitude. The unroofed cell membranes were then immediately fixed for 30 minutes with 2% glutaraldehyde/2% paraformaldehyde (PFA). The cell membranes were sequentially treated with 1% OsO4, 1.5% tannic acid and 1% uranyl acetate before dehydration via successive ethanol baths, which was ultimately substituted with hexamethyldisilazane (HMDS) (#C16700-250; LFG Distribution).

bioRxiv preprint doi: https://doi.org/10.1101/2022.09.27.509635; this version posted September 1, 2023. The copyright holder for this preprint (which was not certified by peer review) is the author/funder. All rights reserved. No reuse allowed without permission.

For immunogold labelling, sonicated plasma membranes were fixed with 4% PFA before incubation with primary (GFP Thermo Fisher A11122 Rabbit 1/20) and secondary antibodies coupled to gold beads (rabbit-gold 815.011 AURION goat 1/25), and the membranes were then incubated with a $NaBH_4$ solution to inactivate aldehydes. The membranes were finally fixed with 2% glutaraldehyde and subjected to the same treatment as that used for morphology studies. The dehydrated samples were metalized via rotary metallization. The coverslips were placed in the chamber of a metallizer (ACE600, Leica Microsystems). Once under a high vacuum ($>10^{-5}$ mBar), the membranes were covered with 2 nm of platinum stabilized by 4 to 6 nm of braided carbon. The resulting platinum replicas were separated from the glass by flotation on acid, washed several times in distilled water baths containing 0.1% detergent (one drop in 10 mL, Photo-Flo, Kodak), and placed on electron microscopy (EM) grids covered with a carbon film (200 mesh formvar/carbon, LFG Distribution). The grids were mounted in the goniometer with eucentric side entry of a transmission electron microscope operating at 80 kV (CM120, Philips), and images were recorded with a Morada digital camera (Olympus). The images were processed by ImageJ software to adjust brightness and contrast and are presented in reverse contrast.

RhoA mono-ADP-ribosylation assay

HUVECs were seeded at a density of 27,000 cells/cm^2 transfected with siCTRL, siCAV1 and siPTRF and then left untreated or treated with ExoC3. Cells were lysed in ADP-ribosylation buffer (20 mM Tris-HCl, 1 mM EDTA, 1 mM DTT, 5 mM $MgCl_2$ and cOmplete protease inhibitor EDTA-free (Roche), pH 7.5) and passed through a 27G syringe 20 times. Cell lysates were collected by centrifugation at 12,000 g for 10 min, and the protein concentration was determined by BCA assay (Thermo Fisher Scientific). The reaction was carried out by incubating 20 µg of cell lysate with 2 µg of ExoC3 and 10 µM 6-biotin-17-NAD$^+$ (BioLog) at 37 °C for 30 min. The reaction was terminated by the addition of 1 mM DTT and Laemmli buffer (0.3 M Tris-HCl, 10% SDS, 37.5% glycerol and 0.4 mM bromophenol blue) and boiling at 100 °C for 5 min. The samples were subjected to 12% SDS–PAGE, and the proportion of ADP-ribosylated (i.e., biotin-ADPr-RhoA) RhoA in the sample was measured by Western blotting using streptavidin–peroxidase.

Plasma membrane sphere formation and tether extraction

Plasma membrane spheres (PMS) were generated via a protocol adapted from (48). Cells were grown to 60–80% confluence on gelatine-coated 100-mm dishes and incubated for 6–8 h in

bioRxiv preprint doi: https://doi.org/10.1101/2022.09.27.509635; this version posted September 1, 2023. The copyright holder for this preprint (which was not certified by peer review) is the author/funder. All rights reserved. No reuse allowed without permission.

PMS buffer [1.5 mM $CaCl_2$, 1.5 mM $MgCl_2$, 5 mM HEPES, 2 mg/ml glucose, 150 mM NaCl, 10 µM MG132 in PBS (pH 7.4)] to induce membrane swelling of the PMSs. Individual PMSs were aspirated using a casein-passivated micropipette connected to a piezo-stage (PI, Karlsruhe, Germany) for manipulation and to a hydrostatic aspiration control system (67). Micropipettes were made in house with borosilicate capillaries pulled into fine cones using a laser pipette puller (P-2000, Sutter Instrument Co.) and microforged at the desired inner diameter (3-4 µm) as described previously (21). For the extraction of tethers from PMSs, we used optical tweezers built in-house that consisted of a single fixed laser beam (infrared laser wavelength of 1070 nm) focused through a 60X water objective mounted on a confocal microscope (Nikon TE2000 inverted microscope) (68). To pull tethers from PMSs, we coated streptavidin beads (3 µm in diameter, Spherotech) with fibronectin, which allowed the beads to bind to PMSs. A membrane tether was generated by bringing the micropipette-held PMS into contact with a bead trapped by the optical tweezers, and then by moving the PMS away from the bead. After extraction, the tether was held at a constant length between 2 and 5 µm, and tether forces were measured during gradual increase in aspiration pressure and thus PMS tension. At a given membrane tension, the corresponding tether force was measured at least 30 s after the pressure change and when equilibration was established. Analysis was performed as described below. Briefly, for each membrane tether, the tether force (f) was plotted as a function of the square root of the membrane tension ($\sqrt{\sigma}$) calculated using the Laplace law (69) and corrected when the length of the "tongue" of a PMS tether inside the micropipette was shorter than the radius of the pipette (70). For each tether, we determined a force f_0 corresponding to the intercept of the linear regression (f vs. $\sqrt{\sigma}$). To estimate the bending rigidity for PMSs obtained from membranes of cell treated differently (siCRTL, siCAV1 and siPTRF cells), the data obtained for all tethers were pooled and rescaled as $(f-f_0)^2/8\pi^2$ and plotted as a function of membrane tension. The corresponding PMS rigidity was obtained from the slope of the linear fit calculated using Graphpad Prism.

Single-Molecule Localization Microscopy of F-actin

For single-molecule localization microscopy (SMLM) of F-actin, we used 2D STORM. HUVECs were cultured on 1.5 high-performance coverslips coated with 10 µg/mL fibronectin for 2 h at room temperature. Soluble G-actin was pre-extracted (0.25% Triton, 0.1% glutaraldehyde in 80 mM PIPES, 5 mM EGTA, and 2 mM $MgCl_2$, pH 6.8) for 30 s at 37 °C.

bioRxiv preprint doi: https://doi.org/10.1101/2022.09.27.509635; this version posted September 1, 2023. The copyright holder for this preprint (which was not certified by peer review) is the author/funder. All rights reserved. No reuse allowed without permission.

The cells were then treated with glutaraldehyde (0.25% Triton, 0.5% glutaraldehyde in 80 mM PIPES, 5 mM EGTA, 2 mM $MgCl_2$, pH 6.8) for 10 min at 37 °C. Glutaraldehyde was quenched for 7 min at RT (0.1% $NaBH_4$ in PBS). Saturation was reached after 1 h at RT (0.22% gelatine and 0.1% Triton X-100 in PBS, pH 7.3). Actin filaments were stained overnight at 4 °C with phalloidin-AF647 (500 nM in PBS). Cells were then placed in switching buffer freshly prepared before imaging [50 mM Tris, 10 mM NaCl, 10% glucose, 0.5 mg/mL glucose oxidase, 50 µg/mL catalase, and 50-100 mM cysteamine (MEA, pH 8.3)] in the presence of phalloidin A647 (10-50 nM). Super-resolved images were acquired with an Elyra-7 SMLM microscope (Carl Zeiss, Germany) using an N.A =1.4 oil 63x objective (Carl Zeiss, Germany) with 1.518 refractive index oil (Carl Zeiss, Germany) and a pco.edge 4.2 camera system (Excelitas PCO GmbH). All processing analyses were performed with Zen software (Carl Zeiss, Germany). Localization of individual molecules was determined using a peak mask size of 15-pixel diameter and a peak intensity-to-noise ratio between 5 and 6. Drift was corrected using a model-based algorithm from Zen software. Super-resolution images were reconstructed at a 20-nm pixel size.

Mesh analysis of the F-actin network imaged via 2D STORM

To quantify actin mesh size from the super resolution images, we developed an image analysis workflow to reliably segment the delimiting continuous actin filaments. First, we clipped the images to a maximum detection count of 10 and applied a line enhancement filter to suppress short apparent discontinuities by modifying a previously described approach (71). Specifically, the maxima of the mean intensities along line profiles at 15 equally spaced orientations around each pixel were calculated (line length 21 px or approximately 0.4 µm). Subsequently, tube-like structures were extracted from the line-enhanced images by applying a Hessian filter implemented in scikit-image (smoothing width of 2 px) as described previously (72) with results binarized using Otsu thresholding. The obtained masks were subdivided into putative filament segments by defining sections of equal length along the mask's morphological skeleton and assigning each pixel to its nearest segment (the chosen length was 20 px or approximately 0.4 µm). The final actin filament segmentation was performed considering only segments that: 1) were not morphologically connected to at least one other segment, to exclude non-filament detections, or 2) exhibited a mean detection count lower than the super-resolution image Otsu threshold. Finally, the actin meshwork was obtained as the connected components of the inverted actin filament segmentation mask.

bioRxiv preprint doi: https://doi.org/10.1101/2022.09.27.509635; this version posted September 1, 2023. The copyright holder for this preprint (which was not certified by peer review) is the author/funder. All rights reserved. No reuse allowed without permission.

Physical modelling

TEM dynamics were theoretically interpreted based on the generalization of our earlier model, which was used for a single TEM (19,20), to account for the case when several TEMs open simultaneously. This generalization was previously used to interpret the data in (18), and we present it here for completeness. The opening of a TEM is driven by a net force,

$$F_d = 2\sigma - \frac{T}{R}, \tag{1}$$

where σ is the membrane tension, *T* is the line tension, and *R* is the TEM radius. For a model lipid membrane in the entropic regime, membrane tension σ depends on *R*, quantified by the Helfrich's law. Written in a generalized form to describe *N* simultaneous TEMs in the same cell, Helfrich′s law states that:

$$\sigma = \sigma_0 \, exp\left[-\frac{\sum_{i=1}^{N} {R_i}^2}{R_c^2}\right] \tag{2}$$

where $R_c^2 = \left(R_{cell}^2 k_B \hat{T}\right)/(8\pi\kappa)$, R_{cell} is the radius of the cell, k_B is the Boltzmann constant, $\hat{T}$ is the temperature, and κ is the effective bending rigidity of the cell membrane. While rigorously derived for a pure lipid membrane, we assumed that Helfrich′s law is applicable to describe the relationship between the effective membrane tension σ acting on TEMs and the observed projected surface in our cells. Thus, the parameter κ in Eq. 2 is an *effective* bending rigidity that accounts for the role played by protein inclusions and the mechanical contribution of the remaining cytoskeletal elements after cell treatment with the toxin. Moreover, we assumed that an eventual buffering role played by the remaining caveolae can be described through modification of the effective parameters σ_0 and κ.

As discussed by (19), the effective line tension is not a constant; it increases with time due to the formation of an actomyosin cable around the TEM. Stefani et al. described this increase as linear, $T \sim \alpha t$. The dynamics of TEM opening are derived from a balance between the driving force (Eq. 2) and cell–substrate friction. Assuming *N* identical TEMs, this balance is

$$2\sigma_0 R exp\left(-\frac{NR^2}{R_c^2}\right) - \alpha t = \mu R^2 \frac{dR}{dt}, \tag{3}$$

bioRxiv preprint doi: https://doi.org/10.1101/2022.09.27.509635; this version posted September 1, 2023. The copyright holder for this preprint (which was not certified by peer review) is the author/funder. All rights reserved. No reuse allowed without permission.

where μ is the friction coefficient. While this equation can be solved numerically, the following analytical approximation can also be obtained, as derived in (18):

$$x \, exp \, x^2 \approx \frac{8\sigma_0^2\sqrt{N}}{\mu\alpha R_c}, \tag{4}$$

where $x = N^{1/2} R_{max}/R_c$ and R_{max} are the maximum TEM radii. As discussed in (18), for biologically relevant values of the model parameters, Eq. 4 leads to the following approximate estimate of the effective membrane bending rigidity:

$$\kappa \approx \frac{k_B \hat{T}}{8\pi} \frac{A_{cell}}{NA_{max}}. \tag{5}$$

Considering the experimental results shown in Table 2 and using the estimate $\kappa \sim (N{\cdot}A_{max})^{-1}$ based on Eq. 5, we deduced an effective bending rigidity after silencing cavin-1/PTRF. These approximate estimates can be refined using Eq. 4 directly, which also considers variations in membrane tension. The following expression for the bending rigidity is thus obtained:

$$\kappa \approx \frac{k_B \hat{T}}{8\pi} \frac{R_{cell}^2}{NR_{max}^2} \, ln\left(\frac{8\sigma_0^2}{\mu\alpha R_{max}}\right). \tag{6}$$

Eq. 6 is used to obtain the predictions of bending rigidity variations mentioned in the text: a reduction in effective bending rigidity by a factor of approximately 1.2 for siPTRF cell membranes and by a factor of approximately 2.3 for siCAV1 cell membranes, which is equivalent to a 15% decrease for siPTRF and 55% for siCAV1 cell membranes.

Fit of the initial opening speed

For short time intervals, the differential equation for the opening dynamics can be simplified to

$$\mu R^2 \frac{dR}{dt} = 2\sigma_0\left(1 - \frac{R_n}{R}\right), \tag{7}$$

where $R_n = T/(2\sigma_0)$ is the minimal nucleation radius. This equation can be integrated to obtain

$$R_n^2 \, ln\left(\frac{R}{R_n} - 1\right) + R_n R + \frac{R^2}{2} - C = \frac{2\sigma_0}{\mu} t, \tag{8}$$

where C is an integration constant, whose value is such that $R = R_0$ for $t = 0$, with R_0 the unknown nucleated TEM radius, which is larger than the minimal nucleation radius R_n; $R_0 > R_n$. Because all TEM measurements are reflect $R \gg R_0 > R_n$, the dominant term on the far left side is the term proportional to $R^2 = A/\pi$, where A is the TEM area. These considerations yield the following estimate of σ_0:

$$\frac{\sigma_0}{\mu} = \frac{A_2 - A_1}{4\pi\Delta t}, \tag{9}$$

where $\Delta t = 1$ s is the time interval between two acquisitions; A_1 is the TEM area in the first image after TEM opening (taken on average at a time $\Delta t/2$), and A_2 is the TEM area in the second image.

Condition	σ_0 (μN/m)	A_{max} (μm^2)	N (average)	$(N \cdot A_{max})^{-1}$ (μm^{-2})
Control	25 ± 10	8.1 ± 0.5	0.90 ± 0.09	0.137 ± 0.022
siCAV1	50 ± 7	23 ± 4	1.92 ± 0.15	0.023 ± 0.006
siPTRF	29 ± 7	9.3 ± 0.7	1.34 ± 0.11	0.080 ± 0.012

Table 2. Estimate of the variation of mechanical cell parameters between different experimental conditions. The value of the effective membrane tension σ_0 for the control case is obtained from earlier estimates (*65*). The increase in σ_0 for siCAV1 and siPTRF cell membranes is deduced from our experimental data using Eq. 9. The TEM maximum area, A_{max}, is the median not the average value because the median is a more robust estimator in the presence of a few extremely large values. As discussed in the text, the variations in the bending rigidity are roughly proportional to variations in $(N \cdot A_{max})^{-1}$, where N is the average number of TEMs opening simultaneously and A_{max} is the TEM maximum area.

Statistical analysis

Statistical tests were performed using the R Software v4.2.1(R Foundation for Statistical Computing, Vienna, Austria. https://www.R-project.org/), along with packages lme4 (1.1-30) (73), lmerTest (v3.1-3) (74), emmeans (v1.8.0) , except for the F-actin mesh size where the

Prism Software was used. All experiments were repeated at least three times to ensure reproducibility and corresponding variability was accounted for in statistical analyses using mixed-effect regressions, with a random intercept estimated for every technical replicate. In particular, Binomial outcomes (e.g. presence/absence) were analysed using mixed-effect logistic regression. Continuous measurements (e.g. TEM area) were investigated with a Gamma log-link function in a mixed-effect framework. Contrasts between multiple pairs of categorical predictors were calculated through estimated marginal means with Tukey′s correction. P-values were calculated as indicated in the respective figure legends. P-values were considered statistically significant at $P \leq 0.05$. Significance levels are indicated as follows: ns: not significant if $P > 0.05$; * : $P \leq 0.05$; **: $P \leq 0.01$; ***: $P \leq 0.001$; ****: ≤ 0.0001.

Acknowledgements

C. Morel and E. Lemerle were supported by PhD fellowships from the University Paris Cité Doctoral School BioSPC and Sorbonne University Doctoral School complexité du vivant, respectively. We thank Amel Mettouchi, Arnaud Echard, Virginia Ribeiro de Andrade (Institut Pasteur, Paris, France) and Michael Henderson (Institut Pasteur/Institut Curie, Paris France) for technical advice, sharing reagents and for discussions. We thank Pierre Nassoy (LP2N, Bordeaux, France), Francoise Brochard Wyart (Institut Curie, Paris, France), and Anne Blangy (CRBM, CNRS, Montpellier, France) for insightful discussions. We thank Darius Koster for sharing results and for fruitful discussions on tether pulling experiments of plasma membrane spheres. We thank Gaëlle Letort (Department of Developmental and Stem Cell Biology, Institut Pasteur, CNRS UMR 3738) for helpful advice on image analysis. We also thank the UTechS PBI, which is part of the France–BioImaging infrastructure network (FBI) supported by the French National Research Agency (ANR-10-INBS-04; Investments for the Future) and acknowledges support from Institut Pasteur, ANR/FBI, the Région Ile-de-France (program DIM1HEALTH), and the French Government Investissement d'Avenir Programme-Laboratoire d'Excellence ‘Integrative Biology of Emerging Infectious Diseases’ (ANR-10-LABX-62-IBEID) for the use of the Zeiss ELYRA7 microscope.

bioRxiv preprint doi: https://doi.org/10.1101/2022.09.27.509635; this version posted September 1, 2023. The copyright holder for this preprint (which was not certified by peer review) is the author/funder. All rights reserved. No reuse allowed without permission.

References

1. Aird WC. Phenotypic heterogeneity of the endothelium: II. Representative vascular beds. Circ Res. 2007 Feb 2;100(2):174–90.

2. Aird WC. Phenotypic heterogeneity of the endothelium: I. Structure, function, and mechanisms. Circ Res. 2007 Feb 2;100(2):158–73.

3. Komarova YA, Kruse K, Mehta D, Malik AB. Protein Interactions at Endothelial Junctions and Signaling Mechanisms Regulating Endothelial Permeability. Circ Res. 2017 Jan 6;120(1):179–206.

4. Guo L, Zhang H, Hou Y, Wei T, Liu J. Plasmalemma vesicle-associated protein: A crucial component of vascular homeostasis. Exp Ther Med. 2016 Sep;12(3):1639–44.

5. Lemichez E, Gonzalez-Rodriguez D, Bassereau P, Brochard-Wyart F. Transcellular tunnel dynamics: Control of cellular dewetting by actomyosin contractility and I-BAR proteins. Biology of the Cell. 2013 Mar;105(3):109–17.

6. Braakman ST, Read AT, Chan DWH, Ethier CR, Overby DR. Colocalization of outflow segmentation and pores along the inner wall of Schlemm’s canal. Exp Eye Res. 2015 Jan;130:87–96.

7. Barzilai S, Yadav SK, Morrell S, Roncato F, Klein E, Stoler-Barak L, et al. Leukocytes Breach Endothelial Barriers by Insertion of Nuclear Lobes and Disassembly of Endothelial Actin Filaments. Cell Reports. 2017 Jan;18(3):685–99.

8. Boyer L, Doye A, Rolando M, Flatau G, Munro P, Gounon P, et al. Induction of transient macroapertures in endothelial cells through RhoA inhibition by Staphylococcus aureus factors. J Cell Biol. 2006 Jun 5;173(5):809–19.

9. Gonzalez-Rodriguez D, Morel C, Lemichez E. Dewetting: From Physics to the Biology of Intoxicated Cells. Adv Exp Med Biol. 2020;1267:101–15.

10. Maddugoda MP, Stefani C, Gonzalez-Rodriguez D, Saarikangas J, Torrino S, Janel S, et al. cAMP signaling by anthrax edema toxin induces transendothelial cell tunnels, which are resealed by MIM via Arp2/3-driven actin polymerization. Cell Host Microbe. 2011 Nov 17;10(5):464–74.

11. Sugai M, Hashimoto K, Kikuchi A, Inoue S, Okumura H, Matsumoto K, et al. Epidermal cell differentiation inhibitor ADP-ribosylates small GTP-binding proteins and induces hyperplasia of epidermis. J Biol Chem. 1992 Feb 5;267(4):2600–4.

12. Chardin P, Boquet P, Madaule P, Popoff MR, Rubin EJ, Gill DM. The mammalian G protein rhoC is ADP-ribosylated by Clostridium botulinum exoenzyme C3 and affects actin microfilaments in Vero cells. EMBO J. 1989 Apr;8(4):1087–92.

13. Paterson HF, Self AJ, Garrett MD, Just I, Aktories K, Hall A. Microinjection of recombinant p21rho induces rapid changes in cell morphology. J Cell Biol. 1990 Sep;111(3):1001–7.

bioRxiv preprint doi: https://doi.org/10.1101/2022.09.27.509635; this version posted September 1, 2023. The copyright holder for this preprint (which was not certified by peer review) is the author/funder. All rights reserved. No reuse allowed without permission.

14. Rolando M, Munro P, Stefani C, Auberger P, Flatau G, Lemichez E. Injection of Staphylococcus aureus EDIN by the Bacillus anthracis Protective Antigen Machinery Induces Vascular Permeability. Infection and Immunity. 2009 Sep 1;77(9):3596–601.

15. Munro P, Benchetrit M, Nahori MA, Stefani C, Clément R, Michiels JF, et al. The Staphylococcus aureus epidermal cell differentiation inhibitor toxin promotes formation of infection foci in a mouse model of bacteremia. Infect Immun. 2010 Aug;78(8):3404–11.

16. Courjon J, Munro P, Benito Y, Visvikis O, Bouchiat C, Boyer L, et al. EDIN-B Promotes the Translocation of Staphylococcus aureus to the Bloodstream in the Course of Pneumonia. Toxins (Basel). 2015 Oct 15;7(10):4131–42.

17. Ng WP, Webster KD, Stefani C, Schmid EM, Lemichez E, Bassereau P, et al. Force-induced transcellular tunnel formation in endothelial cells. MBoC. 2017 Aug 9;28(20):2650–60.

18. Tsai MC, Fleuriot L, Janel S, Gonzalez-Rodriguez D, Morel C, Mettouchi A, et al. DHA-containing phospholipids control membrane fusion and transcellular tunnel dynamics. Journal of Cell Science. 2022 Feb 8;135(5):jcs259119.

19. Gonzalez-Rodriguez D, Maddugoda MP, Stefani C, Janel S, Lafont F, Cuvelier D, et al. Cellular Dewetting: Opening of Macroapertures in Endothelial Cells. Phys Rev Lett. 2012 May 25;108(21):218105.

20. Stefani C, Gonzalez-Rodriguez D, Senju Y, Doye A, Efimova N, Janel S, et al. Ezrin enhances line tension along transcellular tunnel edges via NMIIa driven actomyosin cable formation. Nat Commun. 2017 Jun 23;8:15839.

21. Sinha B, Köster D, Ruez R, Gonnord P, Bastiani M, Abankwa D, et al. Cells Respond to Mechanical Stress by Rapid Disassembly of Caveolae. Cell. 2011 Feb;144(3):402–13.

22. Parton RG, del Pozo MA, Vassilopoulos S, Nabi IR, Le Lay S, Lundmark R, et al. Caveolae: The FAQs. Traffic. 2020 Jan;21(1):181–5.

23. Parton RG, Hanzal-Bayer M, Hancock JF. Biogenesis of caveolae: a structural model for caveolin-induced domain formation. Journal of Cell Science. 2006 Mar 1;119(5):787–96.

24. Porta JC, Han B, Gulsevin A, Chung JM, Peskova Y, Connolly S, et al. Molecular architecture of the human caveolin-1 complex. Sci Adv. 2022 May 13;8(19):eabn7232.

25. Ludwig A, Howard G, Mendoza-Topaz C, Deerinck T, Mackey M, Sandin S, et al. Molecular Composition and Ultrastructure of the Caveolar Coat Complex. PLoS Biol. 2013 Aug 27;11(8):e1001640.

26. Ariotti N, Rae J, Leneva N, Ferguson C, Loo D, Okano S, et al. Molecular Characterization of Caveolin-induced Membrane Curvature. J Biol Chem. 2015 Oct 9;290(41):24875–90.

27. Ludwig A, Nichols BJ, Sandin S. Architecture of the caveolar coat complex. Journal of Cell Science. 2016 Aug 15;129(16):3077–83.

bioRxiv preprint doi: https://doi.org/10.1101/2022.09.27.509635; this version posted September 1, 2023. The copyright holder for this preprint (which was not certified by peer review) is the author/funder. All rights reserved. No reuse allowed without permission.

28. Yang L, Scarlata S. Super-resolution Visualization of Caveola Deformation in Response to Osmotic Stress. J Biol Chem. 2017 Mar 3;292(9):3779–88.

29. Lamaze C, Tardif N, Dewulf M, Vassilopoulos S, Blouin CM. The caveolae dress code: structure and signaling. Curr Opin Cell Biol. 2017 Aug;47:117–25.

30. Daumke O, Lundmark R, Vallis Y, Martens S, Butler PJG, McMahon HT. Architectural and mechanistic insights into an EHD ATPase involved in membrane remodelling. Nature. 2007 Oct;449(7164):923–7.

31. Yeow I, Howard G, Chadwick J, Mendoza-Topaz C, Hansen CG, Nichols BJ, et al. EHD Proteins Cooperate to Generate Caveolar Clusters and to Maintain Caveolae during Repeated Mechanical Stress. Current Biology. 2017 Oct 9;27(19):2951-2962.e5.

32. Nishimura T, Suetsugu S. Super-resolution analysis of PACSIN2 and EHD2 at caveolae. PLOS ONE. 2022 juil;17(7):e0271003.

33. Yu J, Bergaya S, Murata T, Alp IF, Bauer MP, Lin MI, et al. Direct evidence for the role of caveolin-1 and caveolae in mechanotransduction and remodeling of blood vessels. J Clin Invest. 2006 May 1;116(5):1284–91.

34. Del Pozo MA, Lolo FN, Echarri A. Caveolae: Mechanosensing and mechanotransduction devices linking membrane trafficking to mechanoadaptation. Current Opinion in Cell Biology. 2021 Feb;68:113–23.

35. Siddiqui MR, Komarova YA, Vogel SM, Gao X, Bonini MG, Rajasingh J, et al. Caveolin-1–eNOS signaling promotes p190RhoGAP-A nitration and endothelial permeability. Journal of Cell Biology. 2011 May 30;193(5):841–50.

36. Razani B, Engelman JA, Wang XB, Schubert W, Zhang XL, Marks CB, et al. Caveolin-1 Null Mice Are Viable but Show Evidence of Hyperproliferative and Vascular Abnormalities*. Journal of Biological Chemistry. 2001 Oct 12;276(41):38121–38.

37. Miyawaki-Shimizu K, Predescu D, Shimizu J, Broman M, Predescu S, Malik AB. siRNA-induced caveolin-1 knockdown in mice increases lung vascular permeability via the junctional pathway. American Journal of Physiology-Lung Cellular and Molecular Physiology. 2006 Feb;290(2):L405–13.

38. Machado FS, Rodriguez NE, Adesse D, Garzoni LR, Esper L, Lisanti MP, et al. Recent developments in the interactions between caveolin and pathogens. Adv Exp Med Biol. 2012;729:65–82.

39. Spaan AN, Neehus AL, Laplantine E, Staels F, Ogishi M, Seeleuthner Y, et al. Human OTULIN haploinsufficiency impairs cell-intrinsic immunity to staphylococcal alpha-toxin. Science. 2022 Jun 17;376(6599):1285-+.

40. Medina FA, Almeida CJ de, Dew E, Li J, Bonuccelli G, Williams TM, et al. Caveolin-1-Deficient Mice Show Defects in Innate Immunity and Inflammatory Immune Response during Salmonella enterica Serovar Typhimurium Infection. Infection and Immunity. 2006 Dec 1;74(12):6665–74.

41. Dewulf M, Köster DV, Sinha B, Viaris de Lesegno C, Chambon V, Bigot A, et al. Dystrophy-associated caveolin-3 mutations reveal that caveolae couple IL6/STAT3 signaling with mechanosensing in human muscle cells. Nat Commun. 2019 Apr 29;10(1):1974.

42. Lemerle E, Lainé J, Benoist M, Moulay G, Bigot A, Labasse C, et al. Caveolae and Bin1 form ring-shaped platforms for T-tubule initiation. Elife. 2023 Apr 21;12:e84139.

43. Hill MM, Bastiani M, Luetterforst R, Kirkham M, Kirkham A, Nixon SJ, et al. PTRF-cavin, a conserved cytoplasmic protein required for caveola formation and function. Cell. 2008 Jan 11;132(1):113–24.

44. Zlotek-Zlotkiewicz E, Monnier S, Cappello G, Le Berre M, Piel M. Optical volume and mass measurements show that mammalian cells swell during mitosis. J Cell Biol. 2015 Nov 23;211(4):765–74.

45. Helfrich W. Elastic properties of lipid bilayers: theory and possible experiments. Z Naturforsch C. 1973 Dec;28(11):693–703.

46. Raucher D, Sheetz MP. Cell Spreading and Lamellipodial Extension Rate Is Regulated by Membrane Tension. Journal of Cell Biology. 2000 Jan 10;148(1):127–36.

47. Bo L, Waugh RE. Determination of bilayer membrane bending stiffness by tether formation from giant, thin-walled vesicles. Biophys J. 1989 Mar;55(3):509–17.

48. Lingwood D, Ries J, Schwille P, Simons K. Plasma membranes are poised for activation of raft phase coalescence at physiological temperature. Proc Natl Acad Sci U S A. 2008 Jul 22;105(29):10005–10.

49. Derenyi I, Julicher F, Prost J. Formation and Interaction of Membrane Tubes. Phys Rev Lett. 2002 May 28;88(23):238101.

50. Manneville JB, Bassereau P, Lévy D, Prost J. Activity of Transmembrane Proteins Induces Magnification of Shape Fluctuations of Lipid Membranes. Phys Rev Lett. 1999 May 24;82(21):4356–9.

51. Girard P, Prost J, Bassereau P. Passive or Active Fluctuations in Membranes Containing Proteins. Phys Rev Lett. 2005 Mar 1;94(8):088102.

52. Fowler PW, Hélie J, Duncan A, Chavent M, Koldsø H, Sansom MSP. Membrane stiffness is modified by integral membrane proteins. Soft Matter. 2016 Sep 20;12(37):7792–803.

53. Parton RG, Kozlov MM, Ariotti N. Caveolae and lipid sorting: Shaping the cellular response to stress. Journal of Cell Biology. 2020 Apr 6;219(4):e201905071.

54. Roitenberg N, Bejerano-Sagie M, Boocholez H, Moll L, Marques FC, Golodetzki L, et al. Modulation of caveolae by insulin/IGF-1 signaling regulates aging of Caenorhabditis elegans. EMBO Rep. 2018 Aug;19(8):e45673.

55. Rawicz W, Smith BA, McIntosh TJ, Simon SA, Evans E. Elasticity, Strength, and Water Permeability of Bilayers that Contain Raft Microdomain-Forming Lipids. Biophys J. 2008 Jun 15;94(12):4725–36.

bioRxiv preprint doi: https://doi.org/10.1101/2022.09.27.509635; this version posted September 1, 2023. The copyright holder for this preprint (which was not certified by peer review) is the author/funder. All rights reserved. No reuse allowed without permission.

56. Xie K, Yang Y, Jiang H. Controlling Cellular Volume via Mechanical and Physical Properties of Substrate. Biophys J. 2018 Feb 6;114(3):675–87.

57. Carton I, Trouet D, Hermans D, Barth H, Aktories K, Droogmans G, et al. RhoA exerts a permissive effect on volume-regulated anion channels in vascular endothelial cells. American Journal of Physiology-Cell Physiology. 2002 Jul 1;283(1):C115–25.

58. Jansa P, Burek C, Sander EE, Grummt I. The transcript release factor PTRF augments ribosomal gene transcription by facilitating reinitiation of RNA polymerase I. Nucleic Acids Res. 2001 Jan 15;29(2):423–9.

59. Jansa P, Grummt I. Mechanism of transcription termination: PTRF interacts with the largest subunit of RNA polymerase I and dissociates paused transcription complexes from yeast and mouse. Mol Gen Genet. 1999 Oct;262(3):508–14.

60. Liu L, Pilch PF. PTRF/Cavin-1 promotes efficient ribosomal RNA transcription in response to metabolic challenges. Elife. 2016 Aug 16;5:e17508.

61. Shi Y, Tan SH, Ng S, Zhou J, Yang ND, Koo GB, et al. Critical role of CAV1/caveolin-1 in cell stress responses in human breast cancer cells via modulation of lysosomal function and autophagy. Autophagy. 2015;11(5):769–84.

62. Gillet Y, Tristan A, Rasigade JP, Saadatian-Elahi M, Bouchiat C, Bes M, et al. Prognostic factors of severe community-acquired staphylococcal pneumonia in France. Eur Respir J. 2021 Nov;58(5):2004445.

63. Perret M, Badiou C, Lina G, Burbaud S, Benito Y, Bes M, et al. Cross-talk between Staphylococcus aureus leukocidins-intoxicated macrophages and lung epithelial cells triggers chemokine secretion in an inflammasome-dependent manner. Cell Microbiol. 2012 Jul;14(7):1019–36.

64. Tristan A, Bes M, Meugnier H, Lina G, Bozdogan B, Courvalin P, et al. Global Distribution of Panton-Valentine Leukocidin–positive Methicillin-resistant Staphylococcus aureus, 2006. Emerg Infect Dis. 2007 Apr;13(4):594–600.

65. Doye A, Mettouchi A, Bossis G, Clément R, Buisson-Touati C, Flatau G, et al. CNF1 exploits the ubiquitin-proteasome machinery to restrict Rho GTPase activation for bacterial host cell invasion. Cell. 2002 Nov 15;111(4):553–64.

66. Heuser J. The Production of ‘Cell Cortices’ for Light and Electron Microscopy. Traffic. 2000;1(7):545–52.

67. Cuvelier D, Derényi I, Bassereau P, Nassoy P. Coalescence of Membrane Tethers: Experiments, Theory, and Applications. Biophysical Journal. 2005 Apr 1;88(4):2714–26.

68. Sorre B, Callan-Jones A, Manzi J, Goud B, Prost J, Bassereau P, et al. Nature of curvature coupling of amphiphysin with membranes depends on its bound density. PNAS. 2012 Jan 3;109(1):173–8.

69. Evans E, Rawicz W. Entropy-driven tension and bending elasticity in condensed-fluid membranes. Phys Rev Lett. 1990 Apr 23;64(17):2094–7.

bioRxiv preprint doi: https://doi.org/10.1101/2022.09.27.509635; this version posted September 1, 2023. The copyright holder for this preprint (which was not certified by peer review) is the author/funder. All rights reserved. No reuse allowed without permission.

70. Guevorkian K, Gonzalez-Rodriguez D, Carlier C, Dufour S, Brochard-Wyart F. Mechanosensitive shivering of model tissues under controlled aspiration. Proceedings of the National Academy of Sciences. 2011 Aug 16;108(33):13387–92.

71. Al Jord A, Letort G, Chanet S, Tsai FC, Antoniewski C, Eichmuller A, et al. Cytoplasmic forces functionally reorganize nuclear condensates in oocytes. Nat Commun. 2022 Aug 29;13(1):5070.

72. Walt S van der, Schönberger JL, Nunez-Iglesias J, Boulogne F, Warner JD, Yager N, et al. scikit-image: image processing in Python. PeerJ. 2014 Jun 19;2:e453.

73. Bates D, Mächler M, Bolker B, Walker S. Fitting Linear Mixed-Effects Models Using lme4. Journal of Statistical Software. 2015 Oct 7;67:1–48.

74. Kuznetsova A, Brockhoff PB, Christensen RHB. lmerTest Package: Tests in Linear Mixed Effects Models. Journal of Statistical Software. 2017 Dec 6;82:1–26.

bioRxiv preprint doi: https://doi.org/10.1101/2022.09.27.509635; this version posted September 1, 2023. The copyright holder for this preprint (which was not certified by peer review) is the author/funder. All rights reserved. No reuse allowed without permission.

FIGURES AND TABLES

bioRxiv preprint doi: https://doi.org/10.1101/2022.09.27.509635; this version posted September 1, 2023. The copyright holder for this preprint (which was not certified by peer review) is the author/funder. All rights reserved. No reuse allowed without permission.

Figure 1

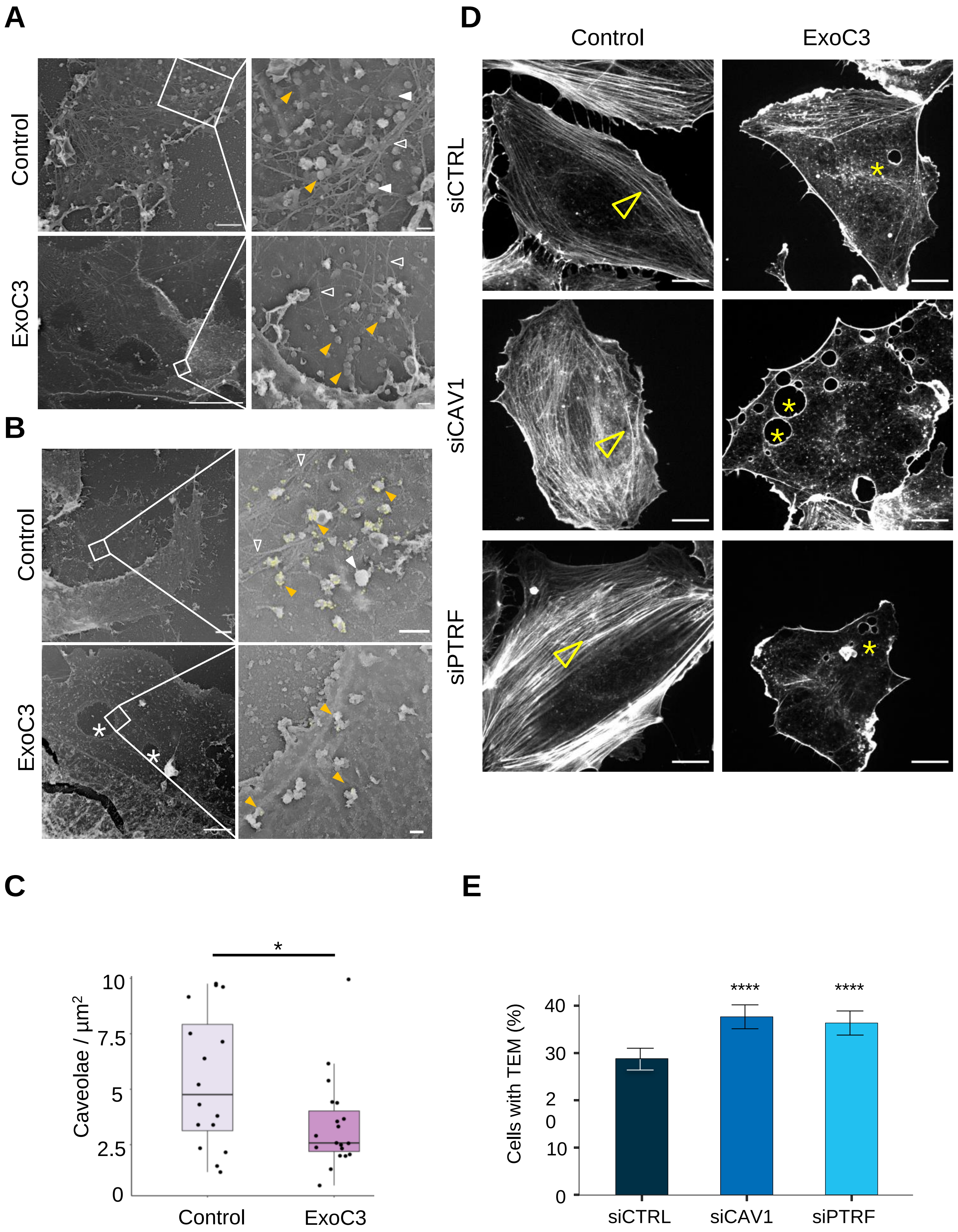

bioRxiv preprint doi: https://doi.org/10.1101/2022.09.27.509635; this version posted September 1, 2023. The copyright holder for this preprint (which was not certified by peer review) is the author/funder. All rights reserved. No reuse allowed without permission.

Figure 1. RhoA inhibition decreases the density of caveolae and actin stress fibers

A-B Transmission electron micrographs show unroofed HUVECs that were either left untreated (Control) or treated with 100µg/mL of ExoC3 (ExoC3) for 24 hours. Right panels show membrane areas at higher magnification with: i) invaginated caveolae (yellow arrowhead), ii) clathrin-coated pits and patches (plain white arrowhead), iii) actin filaments (empty white arrowhead), and iv) TEM tunnels in ExoC3-treated cells (white star). Scale bars left panels: 1 µm for control and 5 µm for ExoC3 condition with 200 nm higher magnifications on right panels. B) yellow dots show immunogold-labelled GFP-CAV1.

C Boxplot shows the density of caveolae per µm^2 of plasma determined on electron micrographs. Values analysed with a mixed-effects linear model with random intercept and Tukey′s correction for pairwise comparison. $^*P = 0.027$ (n=16 cells from 3 technical replicates).

D Confocal spinning disk images show F-actin cytoskeleton of HUVECs left untreated (Control) or treated with 100µg/mL ExoC3 (ExoC3) overnight after 24h of transfection with siRNA control (siCTRL), targeting caveolin-1 (siCAV1) or cavin-1 (siPTRF). Cells were stained with phalloidin-TRITC. Arrowheads show stress fibres and stars show transcellular tunnels bounded by F-actin. Scale bars, 20 µm.

E Histograms show the percentages of ExoC3-treated cells displaying at least one TEM (n=1,400 cells, 8 independent experiments). Error bars show normal asymptotic 95% confidence intervals (CI). Data analysis with mixed-effect logistic regression model with correction for multiple comparisons using a Tukey′s HSD test. $^{****}P<0.0001$, for both siCTRL vs siCAV1 and siCTRL vs siPTRF conditions with no difference between siCAV1 and siPTRF conditions.

bioRxiv preprint doi: https://doi.org/10.1101/2022.09.27.509635; this version posted September 1, 2023. The copyright holder for this preprint (which was not certified by peer review) is the author/funder. All rights reserved. No reuse allowed without permission.

Figure 2

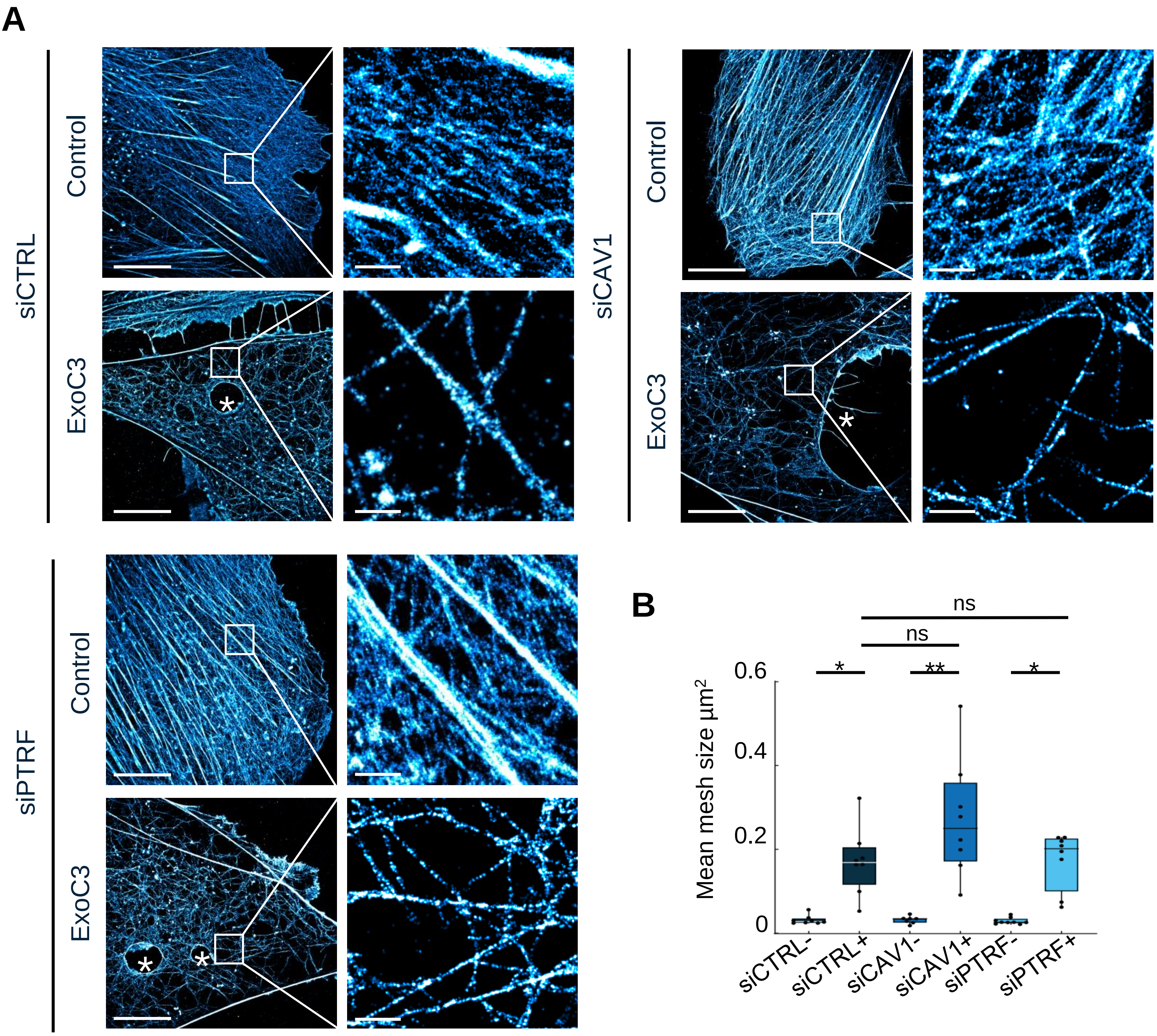

bioRxiv preprint doi: https://doi.org/10.1101/2022.09.27.509635; this version posted September 1, 2023. The copyright holder for this preprint (which was not certified by peer review) is the author/funder. All rights reserved. No reuse allowed without permission.

Figure 2. RhoA inhibition decreases F-actin mesh size with no significant effect of caveolae components

A 2D STORM images show the disruption of actin bundles and intertwined F-actin in cells intoxicated with ExoC3 at 100µg/mL for 24 hours. HUVECs either left untreated or treated with ExoC3 before F-actin staining with phalloidin-AF647. Scale bar, 10 µm. High magnification images are shown in the right panels. Scale bar, 1 µm.

B Boxplot shows the average mesh size per cell (µm²) of the F-actin network. Quantification was performed with 2D STORM images of control (-) and ExoC3-treated cells (+) that were first treated with siCTRL, siCAV1 and siPTRF. $^{**}P<0.01$, $^{*}P<0.05$ calculated with a nested t test ($n=8$ to 9 cells per group, 3 independent replicates).

bioRxiv preprint doi: https://doi.org/10.1101/2022.09.27.509635; this version posted September 1, 2023. The copyright holder for this preprint (which was not certified by peer review) is the author/funder. All rights reserved. No reuse allowed without permission.

Figure 3

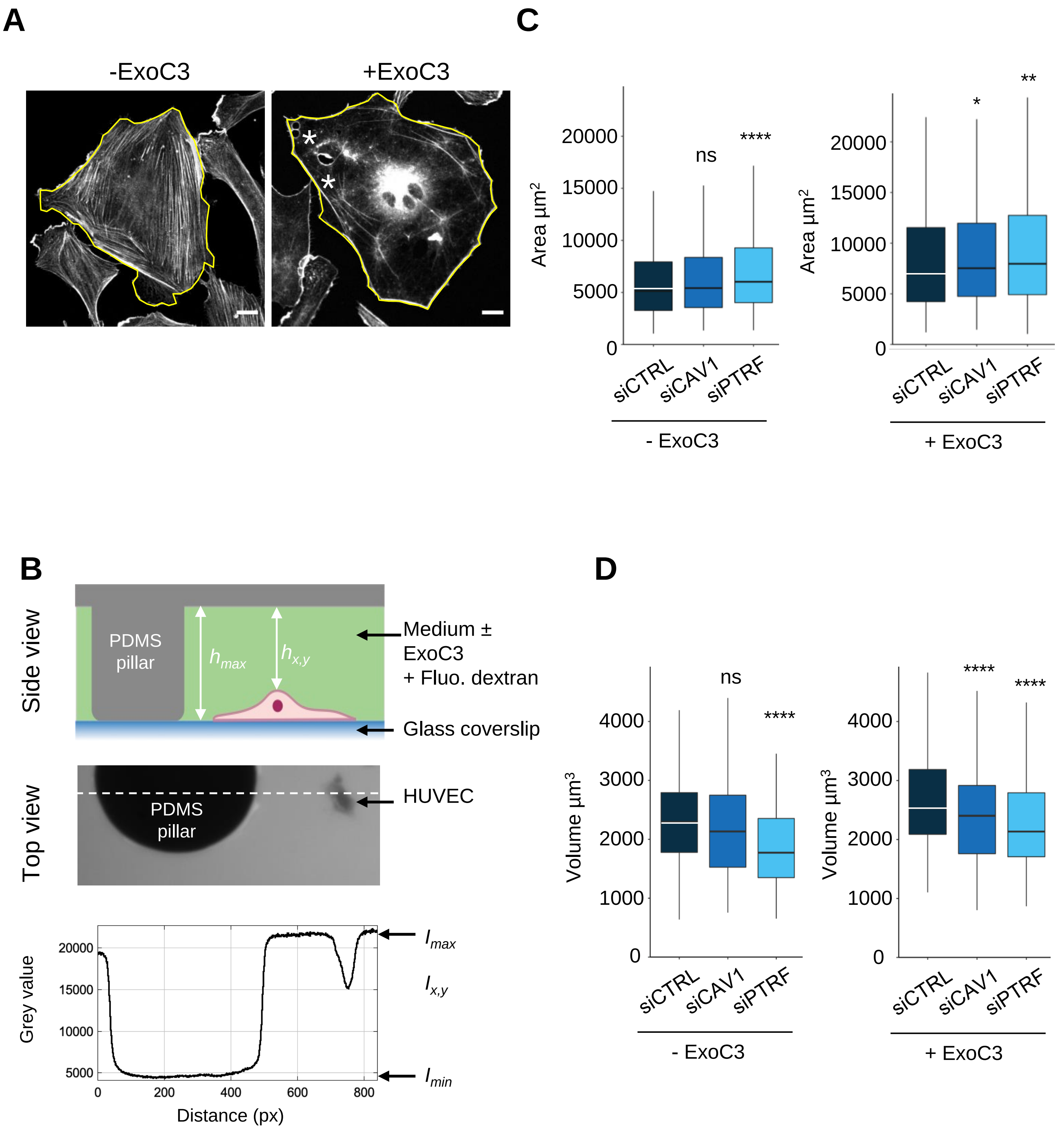

Figure 3. Regulation of HUVEC area and volume by cavin-1/PTRF, caveolin-1 and RhoA.

A Confocal spinning disk images of HUVECs stained with phalloidin-FITC and selected perimeters (yellow line) in the absence (- ExoC3) or presence of ExoC3 (+ ExoC3). Stars show presence of TEMs in ExoC3-treated cells. Scale bar, 20 µm.

B Schematic representation of the microfluidic chamber used to measure cell volume by fluorescence exclusion. Briefly, from the top i) side view of the chamber in which a cell adheres to a coverslip. The PDMS pillar sustains the ceiling (grey), and the maximal height of the chamber h_{max} (background) is known. The siCTRL, siCAV1 or siPTRF transfected HUVECs were seeded in the chamber and remained either untreated or treated with ExoC3. High molecular weight dextran-FITC (green) was added to the chamber and is non permeant to cells (values $h_{x,y}$); ii) raw epifluorescence image showing a typical field of HUVEC; and iii) the graph of fluorescence intensities (in greyscale) show the function of distance along the dotted line. Parameters I_{max} and I_{min} yield values of maximum and minimum fluorescence intensities. Values for cell volume (V_{cell}) were obtained by integrating the fluorescence intensities $h_{max} – h_{x,y}$ over the cell area.

C Boxplots show the distribution of TEM areas values estimated from measures of their perimeters, which is shown in (A). Measurements were performed with HUVEC transfected with siCTRL, siCAV1 or siPTRF and then treated with ExoC3 (+ ExoC3) or untreated (-ExoC3). Measurements were performed with *n*>698 untreated cells and *n*>595 treated cells, 5 independent experiments. **D**) Boxplots show the distribution of cell volumes, as described in (B). Measurements were performed on HUVEC transfected with siCTRL, siCAV1 or siPTRF and then treated with ExoC3 (+ ExoC3) or untreated (- ExoC3). Data are from *n*=216 and *n*=308 cells after siCTRL ±ExoC3 treatment, *n*=197 and *n*=266 cells after siCAV1 ±ExoC3 treatment and *n*=152 and *n*=157 cells after siPTRF 10 ±ExoC3 treatment; 3 independent experiments.

D Graph shows technical replicates pooled together. The data were analysed with a mixed-effect generalized linear model with Gamma log-link function, random intercept accounting for technical variability and Tukey′s correction for pairwise comparisons between control and each siRNA treatment, ****$P<0.0001$, **$P<0.01$, *$P<0.05$ and ns, not significant.

bioRxiv preprint doi: https://doi.org/10.1101/2022.09.27.509635; this version posted September 1, 2023. The copyright holder for this preprint (which was not certified by peer review) is the author/funder. All rights reserved. No reuse allowed without permission.

Figure 4

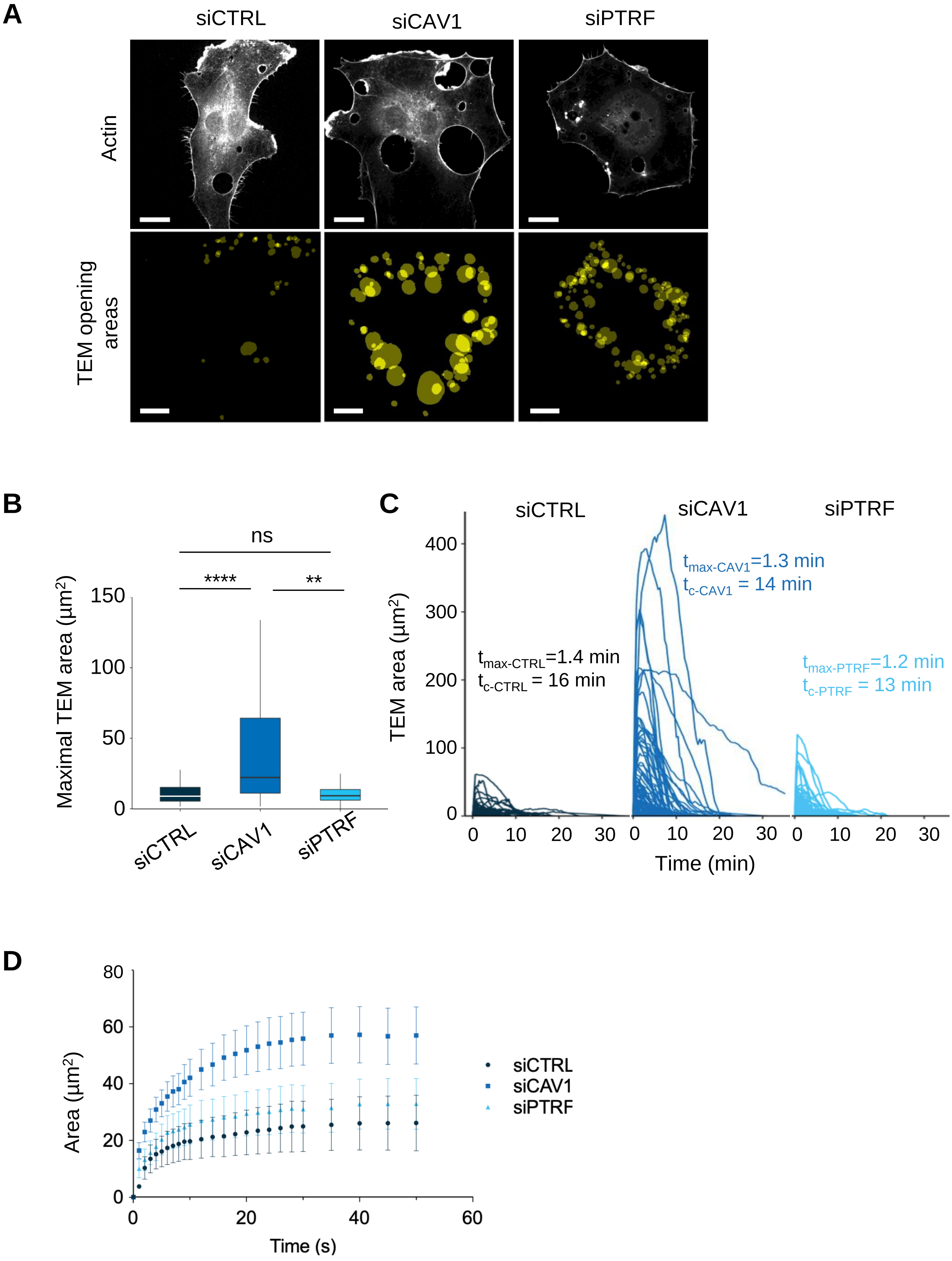

bioRxiv preprint doi: https://doi.org/10.1101/2022.09.27.509635; this version posted September 1, 2023. The copyright holder for this preprint (which was not certified by peer review) is the author/funder. All rights reserved. No reuse allowed without permission.

Figure 4. Caveolin-1 controls the TEM opening speed and maximum size.

A Images show examples of projections of all tunnels upon TEM initial opening (lower panel) in HUVECs transfected with Lifeact-GFP expression plasmid and siCTRL, siCAV1 or siPTRF captured during 1 h of live imaging. Lifeact-GFP HUVECs transfected with different siRNAs were treated with ExoC3 and recorded by live imaging for 1 h. All initial TEM opening was based on the first frame in which TEM tunnels formed using ICY. The lower panel shows the projection of cumulative areas of initial TEM opening identified during 1 h of live imaging. Scale bars, 20 µm. **B** Boxplot shows the distribution of TEMs, the maximal and median area values in HUVECs cotransfected with Lifeact-GFP expressing plasmid and siCTRL, siCAV1, or siPTRF prior ExoC3 treatment. Maximal areas were determined based on each kinetic parameter of TEM dynamics, as shown in (C). The data represent *n*>105 TEMs in 7 cells of each treatment group from >3 independent experiments. Graph shows technical replicates pooled together. Statistical data analysis using a mixed-effect generalized linear model with Gamma log-link function, random intercept, and Tukey′s correction for multiple comparisons. ****P<0.0001, **P<0.01 and ns, non-significant.

C The graph shows variations in TEM areas as a function of time expressed in minutes. HUVECs transfected with siCTRL, siCAV1 or siPTRF were treated with ExoC3 for 24 h. The calculated values of t_{max} that corresponded to the time of opening to the time when the maximal areas were observed and the values of t_c corresponded to the time frame of a complete cycle of opening and closing are indicated on the graph for each condition. The data are from *n*>105 TEMs of 7 cells per treatment from >3 independent experiments.

D Graph shows variations in mean values, expressed in seconds, in the TEM areas of cells treated with ExoC3. The curves were plotted with data obtained from time-lapse video recorded at 1 frame/second for 30 min. Lifeact-GFP expressing cells transfected with siCTRL, siCAV1, and siPTRF. The data correspond to *n*> 22 TEMs per condition from 4 independent experiments.

bioRxiv preprint doi: https://doi.org/10.1101/2022.09.27.509635; this version posted September 1, 2023. The copyright holder for this preprint (which was not certified by peer review) is the author/funder. All rights reserved. No reuse allowed without permission.

Figure 5

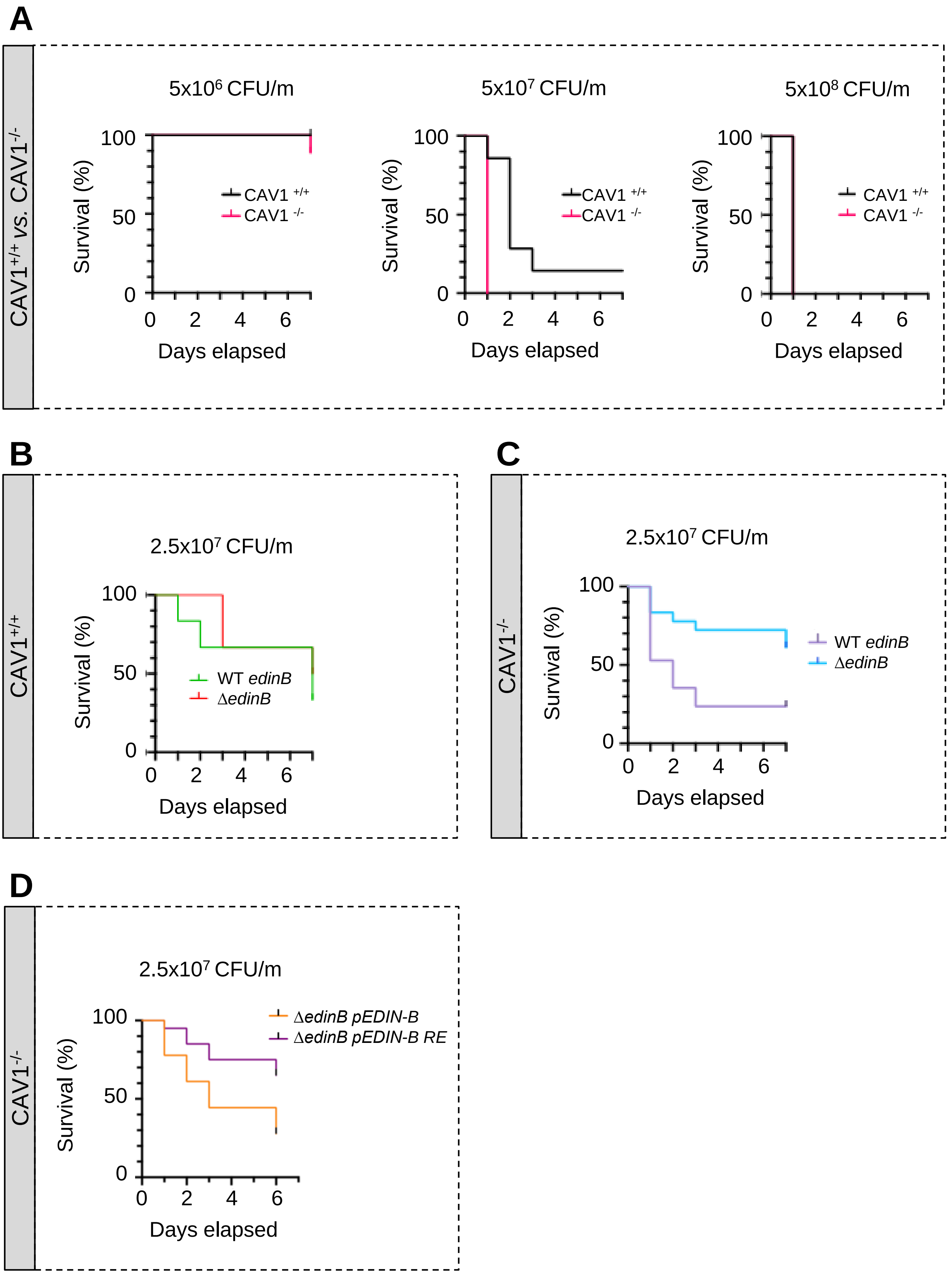

bioRxiv preprint doi: https://doi.org/10.1101/2022.09.27.509635; this version posted September 1, 2023. The copyright holder for this preprint (which was not certified by peer review) is the author/funder. All rights reserved. No reuse allowed without permission.

Figure 5. Hyper-susceptibility of Cav1-deficient mice to EDIN-B mART activity on RhoA

A-D Kaplan–Meier survival curves over 7 days for CAV1$^{-/-}$ mice and/or CAV1$^{+/+}$ littermates infected intravenously at day 0 with isogenic strains of *Staphylococcus aureus* and doses, expressed as colony-forming units per mouse (CFU/m).

A Mice were challenged by intravenous injection of 5×10^6 CFU/mouse (group of 10 CAV1$^{+/+}$ mice vs. group of 9 CAV1$^{-/-}$ mice), 5×10^7 CFU/mouse (group of 7 CAV1$^{+/+}$ mice vs. group of 9 CAV1$^{-/-}$ mice) or 5×10^8 CFU/mouse (group of 7 CAV1$^{+/+}$ mice vs. group of 8 CAV1$^{-/-}$ mice). Data show a significant increase of CAV1$^{-/-}$ lethality when challenged with 5×10^7 CFU/mouse. Log-rank test (Mantel–Cox), $P < 0.0011$ at 5×10^7 CFU/mouse (n=1 experiment).

B-C Mouse lethal doses 50 (LD$_{50}$) of WT *edinB* or Δ*edinB* strains established in CAV1$^{+/+}$ mice (B) and CAV1$^{-/-}$ mice (C). B) CAV1$^{+/+}$ mice injected i.v. with 2.5×10^7 CFU/mouse (group of 12 mice for WT *edinB* and Δ *edinB* strains, n=2 independent experiments). Log-rank test (Mantel–Cox) show no significant difference. C) CAV1$^{-/-}$ mice were injected i.v. with 2.5×10^7 CFU/mouse (groups of 17 or 18 mice for WT *edinB* or Δ*edinB* strains, n=2 independent experiments). Log-rank test (Mantel–Cox) show significant increase of susceptibility of CAV1$^{-/-}$ mice to WT *edinB* compared with Δ*edinB* (P=0.0123).

D Comparative analysis of the susceptibility of CAV1$^{-/-}$ mice to bloodstream infection triggered by *S. aureus* Δ*edinB* complemented with a plasmid encoding wildtype EDIN-B (pEDIN-B) or the catalytically inactive EDIN-B mutant (pEDIN-B RE). Mice were injected with 2.5×10^7 CFU/mouse (groups of 20 CAV1$^{-/-}$ mice for Δ*edinB* pEDIN-B WT and for Δ*edinB* pEDIN-B RE strains, n=2 independent experiments). Log-rank test (Mantel–Cox) shows a higher susceptibility of CAV1$^{-/-}$ mice infected with *S. aureus* expressing catalytically active EDIN-B (P=0.0083).

bioRxiv preprint doi: https://doi.org/10.1101/2022.09.27.509635; this version posted September 1, 2023. The copyright holder for this preprint (which was not certified by peer review) is the author/funder. All rights reserved. No reuse allowed without permission.

Figure 6

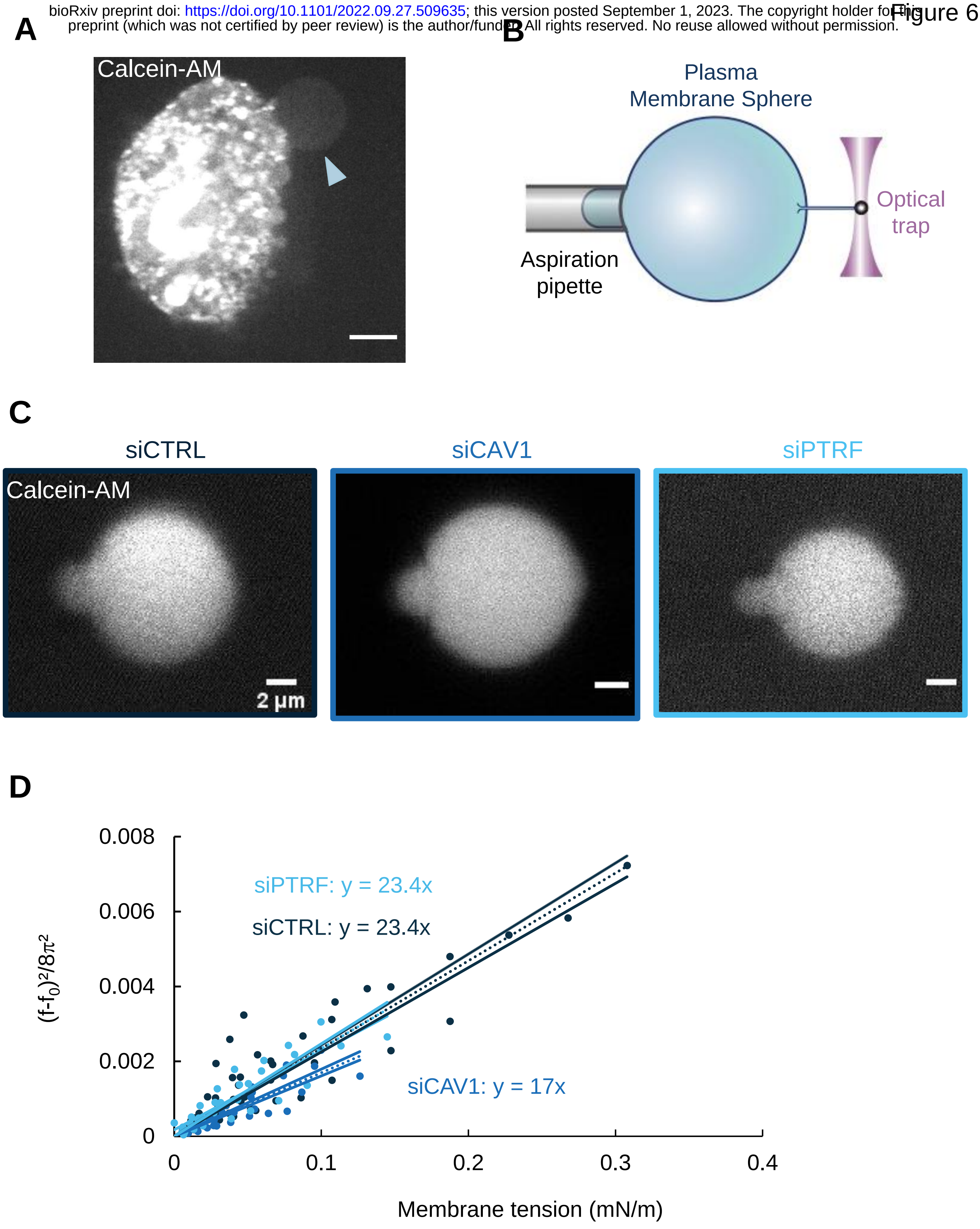

bioRxiv preprint doi: https://doi.org/10.1101/2022.09.27.509635; this version posted September 1, 2023. The copyright holder for this preprint (which was not certified by peer review) is the author/funder. All rights reserved. No reuse allowed without permission.

Figure 6. Caveolin-1 expression is a key determinant of membrane bending rigidity.

A Confocal spinning disk image of a HUVEC displaying a calcein-AM-positive attached plasma membrane sphere (PMS) (arrowhead). Scale bar, 10 µm.

B Schematic representation of the device used for measuring membrane mechanical parameters. It shows micropipette aspiration (grey) of a PMS (blue) and a tube pulled from the PMS through a bead bound to the PMS and trapped with an optical tweezer (purple). Increasing the aspiration pressure in the pipette allowed a progressive increase in the PMS membrane tension.

C Confocal images show examples of calcein-AM-positive PMSs prepared from siCTRL-, siCAV1- or siPTRF-transfected cells during micropipette aspiration. Scale bars, 2 µm.

D The Force required to pull membrane tubes rescaled to $((f-f_0)^2/8\pi^2)$ (in pN^2), which is a function of the membrane tension (mN/m) for different siCTRL, siCAV1 and siPTRF treatments. The force f_0 was measured for each tube as the force when the membrane tension vanishes. The bending rigidity κ (in k_BT) was determined via the slope of the linear regression. The data were calculated from n=5 to n=10 tubes per condition (>4 independent experiments). Linear regression data are shown as dashed lines, and 95% confidence intervals are shown as solid lines (slope ± s.d.). Data recorded between siCTRL and siCAV1 are significant showing no overlap between respective 95% confidence intervals.

bioRxiv preprint doi: https://doi.org/10.1101/2022.09.27.509635; this version posted September 1, 2023. The copyright holder for this preprint (which was not certified by peer review) is the author/funder. All rights reserved. No reuse allowed without permission.

Conditions	**Mean cell area** ***A* (μm²)**	**s.d. of the cell area (μm²)**	**Mean cell volume** ***V* (μm³)**	**s.d. of the cell volume (μm³)**	**Cell height** ***h* (μm)**	**s.d. of the height (μm)**
siCTRL-	6,583	5,168	2,320	3,147	0.35	0.75
siCTRL+	9,025	7,258	2,710	4,326	0.30	0.72
siCAV1-	7,048	5,583	2,146	3,214	0.30	0.70
siCAV1+	9,831	7,984	2,357	3,010	0.24	0.50
siPTRF-	7,539	5,450	1,914	2,234	0.25	0.48
siPTRF+	10,139	7,873	2,282	2,628	0.23	0.43

Table 1: Cell spreading area, volume, and height. The means and standard deviations (s.ds.) of the cell spreading area (Fig. 3C) and volume (Fig. 3D). Cell height was estimated by the ratio between the cell volume and cell area, and the standard deviation was estimated via error propagation.

bioRxiv preprint doi: https://doi.org/10.1101/2022.09.27.509635; this version posted September 1, 2023. The copyright holder for this preprint (which was not certified by peer review) is the author/funder. All rights reserved. No reuse allowed without permission.

SUPPLEMENTARY MATERIALS

bioRxiv preprint doi: https://doi.org/10.1101/2022.09.27.509635; this version posted September 1, 2023. The copyright holder for this preprint (which was not certified by peer review) is the author/funder. All rights reserved. No reuse allowed without permission.

Figure S1

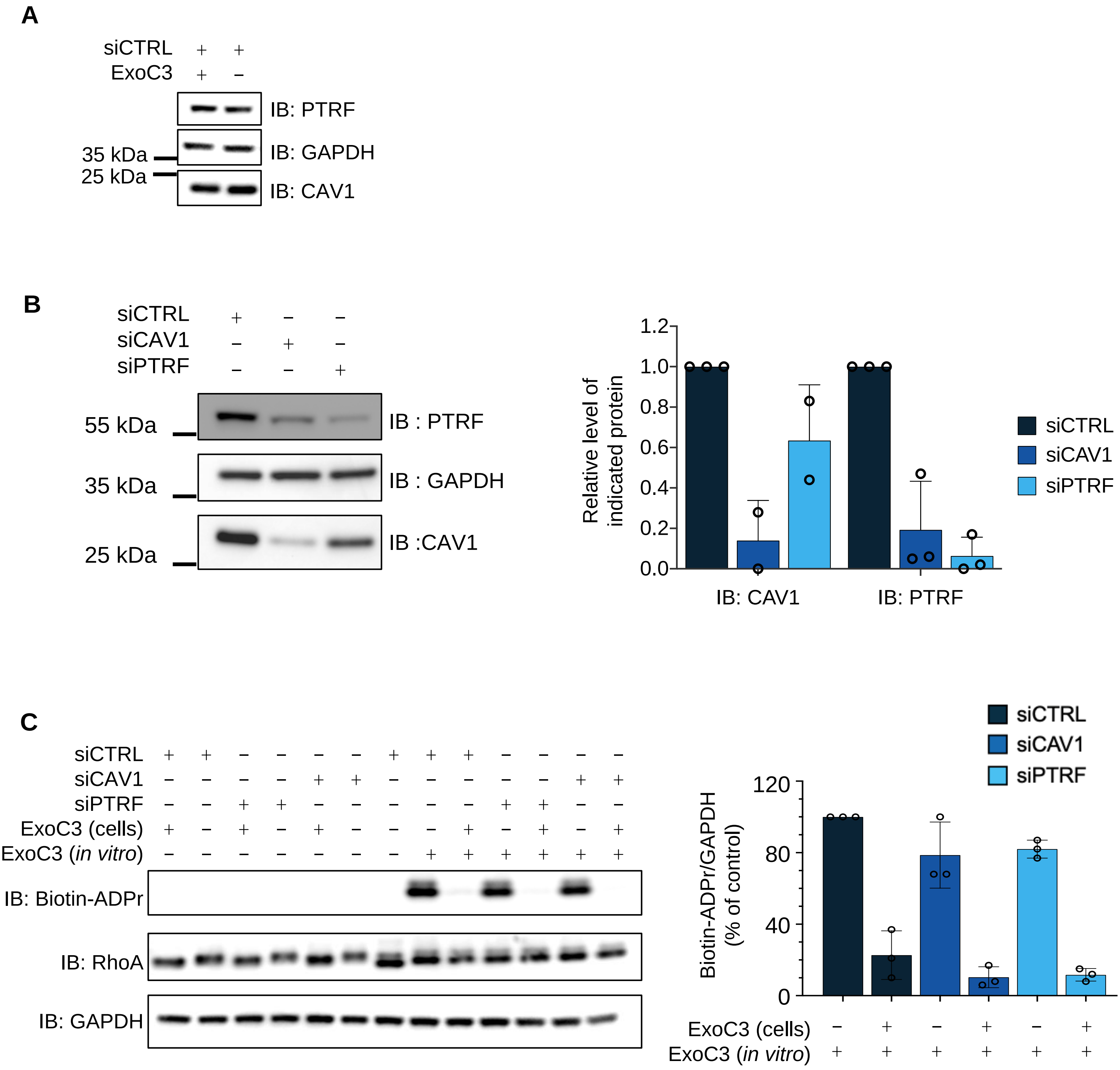

bioRxiv preprint doi: https://doi.org/10.1101/2022.09.27.509635; this version posted September 1, 2023. The copyright holder for this preprint (which was not certified by peer review) is the author/funder. All rights reserved. No reuse allowed without permission.

Figure S1. Controls of siRNAs and RhoA ADP-ribosylation efficacies.

A Immunoblots show caveolin-1 (IB: CAV1) and cavin-1/PTRF (IB: PTRF) in total cellular extracts of HUVECs transfected with siCTRL and then treated for 24 h with ExoC3. Immunoblot GAPDH (IB: GAPDH) was used as the loading control. Immunoblots are representative of 3 independent experiments.

B Immunoblots of caveolin-1 (IB: CAV1) and cavin-1/PTRF (IB: PTRF) show the specific and cross-depletion effects of siCAV1 and siPTRF. Immunoblot anti-GAPDH antibody (IB: GAPDH) shows equal loading. The graph shows caveolin-1 and cavin-1/PTRF levels normalized to the level of GAPDH (3 independent experiments).

C Western blots show the fraction of ADP-ribosylated RhoA in cells that were resistant to a second round of in vitro ADP-ribosylation with biotin-NAD+. Western blot shows the fraction of ADP-ribosylated RhoA in vitro as detected with streptavidin–peroxidase (IB: Biotin-ADPr) i.e. not modified during cell intoxication. Immunoblotting with an anti-RhoA antibody (IB: RhoA) revealed equal RhoA protein levels. Immunoblotting with an anti-GAPDH antibody revealed equal protein loading. Blots are representative of n=3 independent experiments. The graph shows the mean values of the blot signal intensities ± s.ds. from n=3 independent experiments. Values correspond to the signal intensities of biotin-tagged ADP-ribosylated RhoA (Biotin-ADPr) normalized to those of RhoA and GAPDH IB signals. Values are expressed as a percentage compared with the intensity of the siCTRL-transfected untreated cells, which was set to 100%.

bioRxiv preprint doi: https://doi.org/10.1101/2022.09.27.509635; this version posted September 1, 2023. The copyright holder for this preprint (which was not certified by peer review) is the author/funder. All rights reserved. No reuse allowed without permission.

Figure S2

A ExoC3 treatment

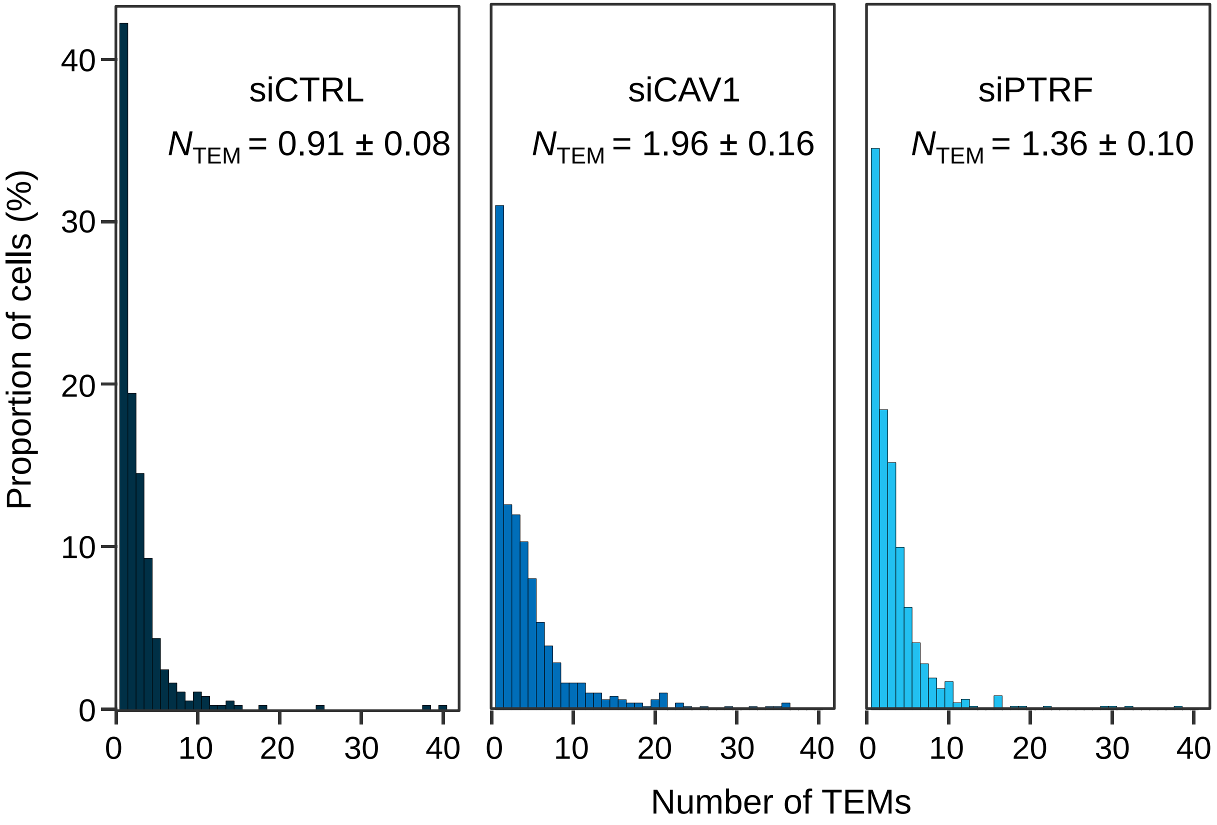

B EDIN treatment

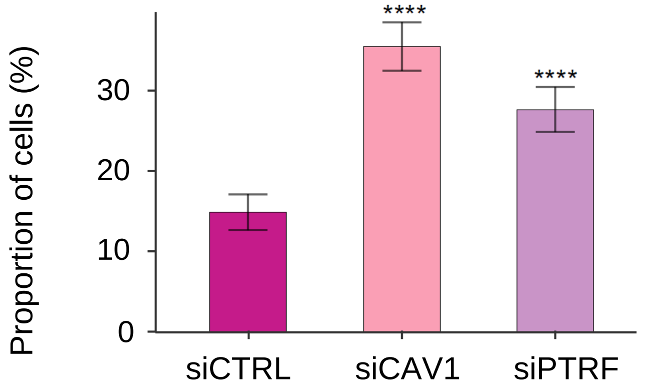

C EDIN treatment

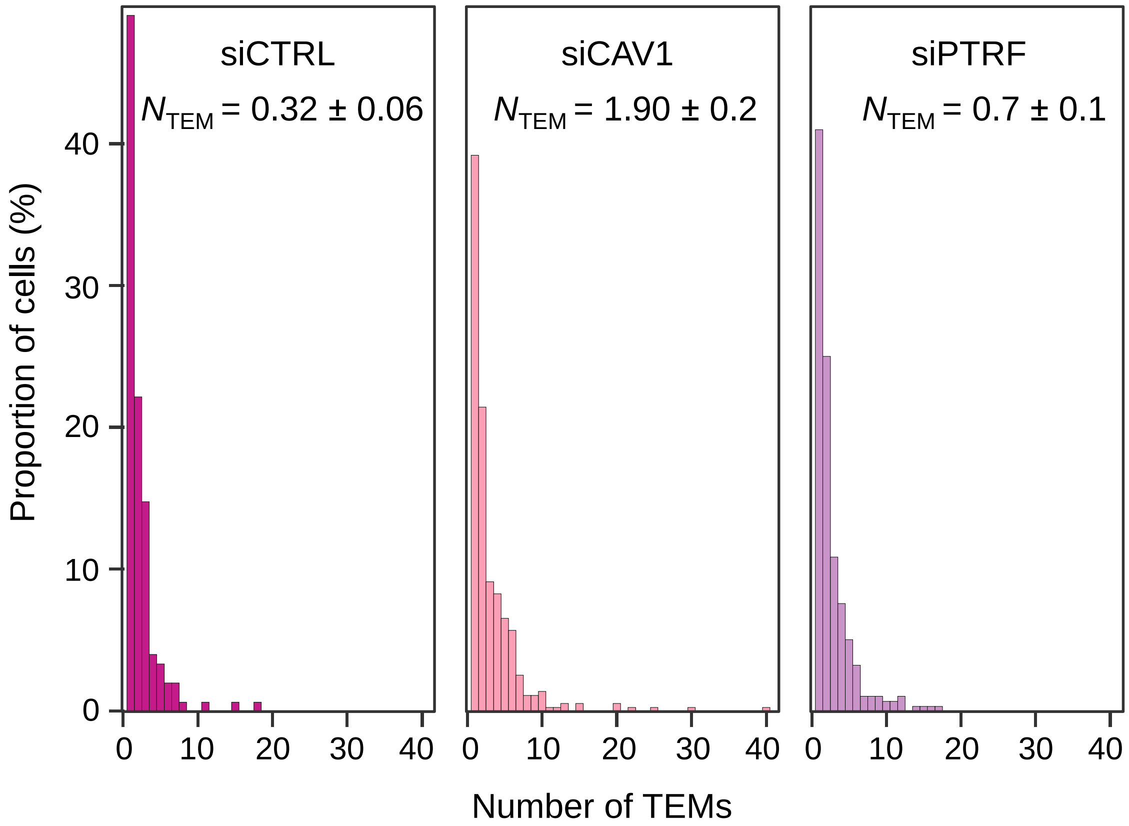

bioRxiv preprint doi: https://doi.org/10.1101/2022.09.27.509635; this version posted September 1, 2023. The copyright holder for this preprint (which was not certified by peer review) is the author/funder. All rights reserved. No reuse allowed without permission.

Figure S2. Caveolin-1 and cavin-1/PTRF depletion increases TEM formation in both ExoC3- and EDIN-treated cells.

A The graph shows the distribution of HUVECs between classes defined by TEM tunnel density ranging from a group of cells displaying only 1 TEM and those for which the density increased by a factor of 1 through those cells with 40 TEMs (y-axis). HUVECs were transfected with siCTRL, siCAV1 or siPTRF before treatment with ExoC3. The graph includes the geometric means (N_{TEM}) of the density of TEMs per cell within the whole cell population ± s.d. Graph shows technical replicates pooled together. Statistical data analysis using a mixed-effect linear model, with random intercept shows significant differences between values of N_{TEM}, ****P<0.0001. Data from *n*=1,400 cells per condition from 7 independent experiments.

B Histograms show the percentages of EDIN-treated cells with at least one TEM (n=986 cells per treatment in 5 independent experiments). Error bars show 95% confidence intervals (CIs). Data analysis with a logistic regression model adjusted for multiple comparisons using Tukey's HSD test, ****P<0.0001; the siCTRL vs. siCAV1 groups and the siCTRL vs. siPTRF groups. No difference was recorded between the siCAV1 and siPTRF groups.

C The graph shows the distribution of HUVECs between classes as defined by TEM density with ranging from a group of cells displaying only 1 TEM and those for which the density increased by a factor of 1 through those cells with 40 TEMs (y-axis). HUVECs were transfected with siCTRL, siCAV1 or siPTRF before treatment with ExoC3. The graph includes values the geometric means (N_{TEM}) of the density of TEMs per cell within the whole cell population ± s.d. Statistical data analysis was based on a mixed linear model with a random intercept and fixed effects and revealed significant differences between N_{TEM} values, ****P<0.0001 (n >986 cells per condition from 5 independent experiments).

bioRxiv preprint doi: https://doi.org/10.1101/2022.09.27.509635; this version posted September 1, 2023. The copyright holder for this preprint (which was not certified by peer review) is the author/funder. All rights reserved. No reuse allowed without permission.

Figure S3

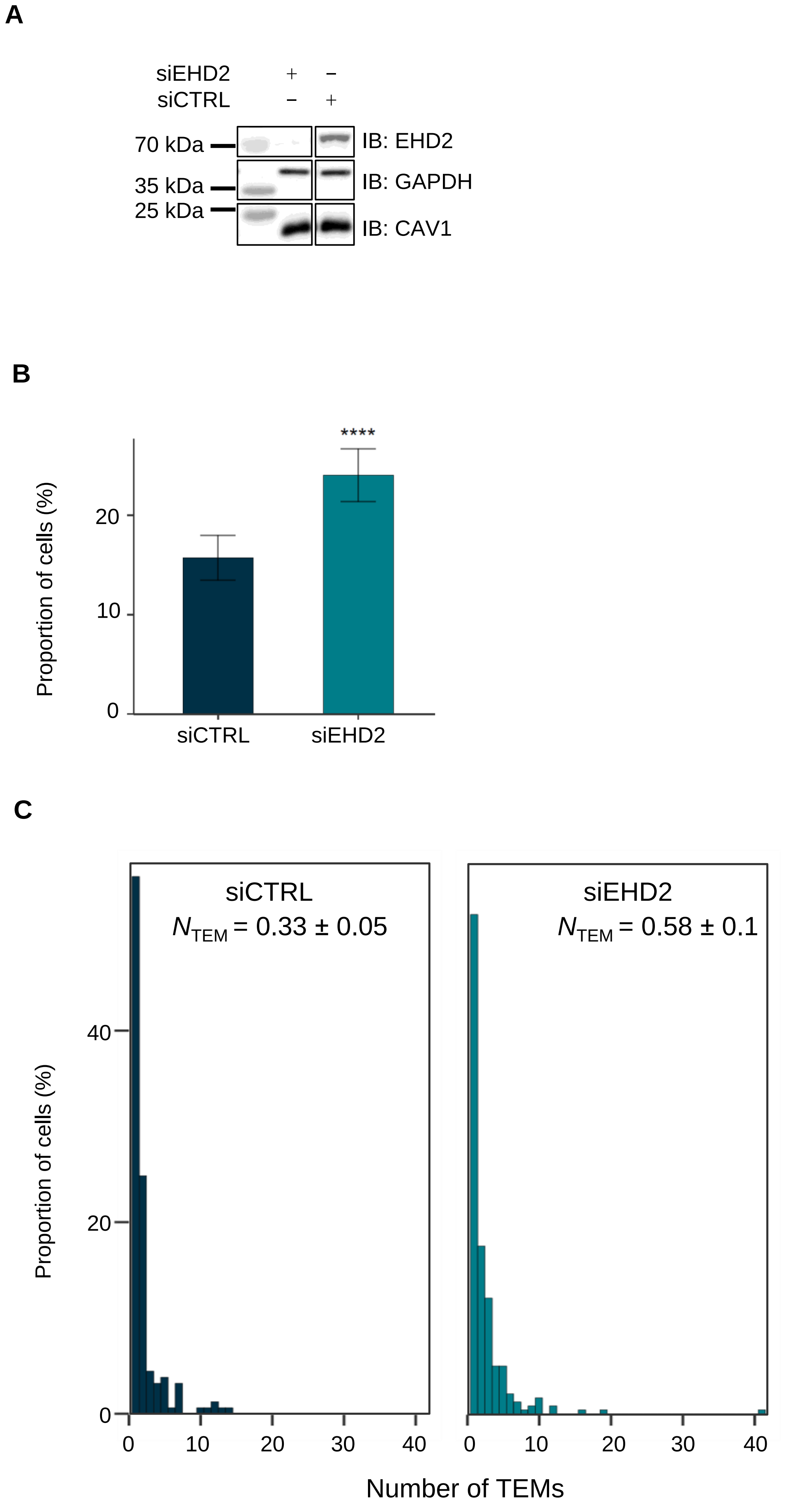

bioRxiv preprint doi: https://doi.org/10.1101/2022.09.27.509635; this version posted September 1, 2023. The copyright holder for this preprint (which was not certified by peer review) is the author/funder. All rights reserved. No reuse allowed without permission.

Figure S3. Depletion of the caveolar accessory component EHD2 increases TEM formation.

A Immunoblots show EHD2 cellular levels (IB: EHD2) in total cellular extracts of HUVECs transfected with siCTRL or siEHD2 and then treated for 24 h with ExoC3. Immunoblot GAPDH (IB: GAPDH) was used as the loading control. Immunoblots are representative of n=3 independent experiments.

B Histograms show the percentages of C3-treated cells displaying at least one TEM (n=1000 cells per condition from 5 independent experiments). Error bars show 95% confidence intervals (CIs). Data analysis with a logistic regression model adjusted for multiple comparisons using Tukey’s HSD test, ****P<0.0001 for the siCTRL versus siEHD2 groups.

C The graph shows the distribution of HUVECs between classes as defined by TEM density ranging from a group of cells displaying only 1 TEM and those for which the density increased by a factor of 1 through those cells with 40 TEMs/cell (y-axis). HUVECs were transfected with siCTRL or siEHD2 before treatment with ExoC3. The graph includes values of the geometric means (N_{TEM}) of the density of TEMs per cell within the whole cell population ± s.d. Statistical data analysis was based on a mixed linear model with a random intercept and fixed effects and revealed significant differences between N_{TEM} values, ****P<0.0001 (n= 1000 cells per condition from 5 independent experiments).

bioRxiv preprint doi: https://doi.org/10.1101/2022.09.27.509635; this version posted September 1, 2023. The copyright holder for this preprint (which was not certified by peer review) is the author/funder. All rights reserved. No reuse allowed without permission.

Figure S4

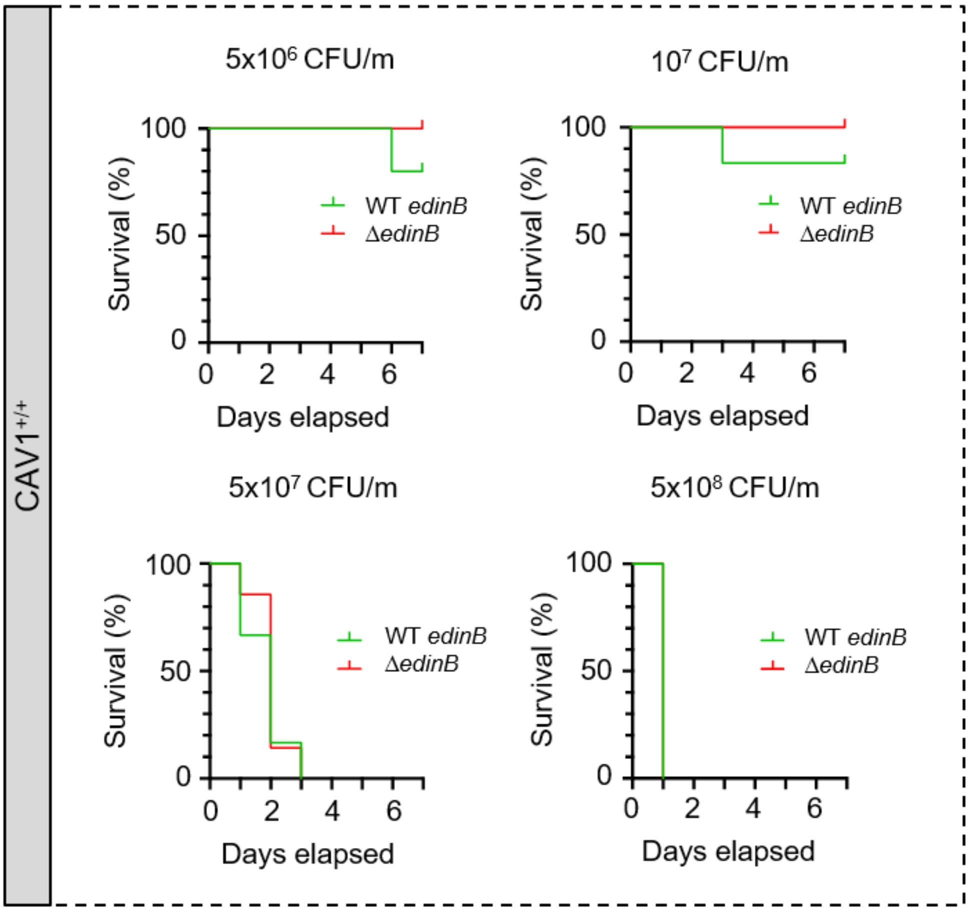

bioRxiv preprint doi: https://doi.org/10.1101/2022.09.27.509635; this version posted September 1, 2023. The copyright holder for this preprint (which was not certified by peer review) is the author/funder. All rights reserved. No reuse allowed without permission.

Figure S4. CAV1+/+ mice susceptibility to EDIN-B in Staphylococcal septicemia.

Kaplan–Meier survival curves with data obtained through 7 days from groups of CAV1+/+ infected intravenously at Day 0 with different doses of LUG1799 wild-type *S. aureus*, expressed as colony-forming units per mouse (CFU/m). Comparative analysis of CAV1$^{+/+}$ mouse susceptibility to bloodstream infection with either the WT *edinB* or Δ*edinB* strain. Mice were injected with 5×10^{6} CFU/m (n=5 mice infected with the WT *edinB* or Δ*edinB* strain; 1 experiment), 107 CFU/m (n=17 and n=19 mice infected with the WT *edinB* or Δ*edinB* strain, respectively; 3 experiments), 5 ×10^{7} CFU/m (n=19 or n=18 mice infected with the WT *edinB* or Δ*edinB* strain; 3 experiments), and 5×10^{8} CFU/m (n=4 or n=5 mice infected with either the WT or Δ*edinB* strain, respectively; 1 experiment). There were no significant differences in the kinetics of survival between the WT and Δ*edinB*-infected animals, as determined by log-rank test (Mantel–Cox).

Supplementary videos

Visualization of TEM tunnel cycles in a HUVEC that was transfected with GFP-LifeAct (addgene) expressing plasmid and different siRNA control or targeting CAV1 or Cavin1/PTRF (**video 1, 2 and 3** respectively), or prior to intoxication with ExoC3 at 100 µg/ml for 24 hours. Time-lapse video microscopy showing the accumulation of F-actin at the edge TEMs during 1 hour of video recording at 1 frame every 15, 23 and 20.5 seconds respectively and played at seven frames per second. Scale bar, 10 µm.